

## Observations of gravity waves in the middle atmosphere of Mars

<sup>2</sup> WILLIAM R. SAUNDERS ,<sup>1</sup> MICHAEL J. PERSON ,<sup>2</sup> AND PAUL WITHERS <sup>1,3</sup>

<sup>3</sup> *Department of Astronomy, Boston University, Boston, MA 02215, USA*

<sup>4</sup> *Department of Earth, Atmospheric, and Planetary Sciences, Massachusetts Institute of Technology (MIT),*  
<sup>5</sup> *Cambridge, MA 02139-4307, USA.*

<sup>6</sup> *Center for Space Physics, Boston University, Boston, MA 02215, USA*

<sup>7</sup> (Received April 17, 2020; Revised January 5, 2021; Accepted \*\*\*\*\*)

<sup>8</sup> Submitted to AJ

### ABSTRACT

<sup>10</sup> Gravity waves are ubiquitous throughout the atmosphere of Mars. Their propagation  
<sup>11</sup> and dissipation influence the circulation and thermal structure of the middle and upper  
<sup>12</sup> atmosphere. Yet there have been few studies of gravity wave characteristics in the  
<sup>13</sup> middle atmosphere, a region that is critical for their propagation from generation in  
<sup>14</sup> the lower atmosphere to dissipation and associated exchanges of momentum and energy  
<sup>15</sup> in the upper atmosphere. There have been few studies because few atmospheric profiles  
<sup>16</sup> span the middle atmosphere with the vertical resolution of km-scale or smaller that is  
<sup>17</sup> required to characterize gravity waves.

<sup>18</sup> Here we report the characterization of gravity waves in the middle atmosphere using  
<sup>19</sup> twelve high-resolution atmospheric density profiles. Four of these were acquired from a  
<sup>20</sup> ground-based stellar occultation from 1976 that yielded immersion and emersion pro-  
<sup>21</sup> files on opposite sides of the planet and the remaining eight were measured during

22 atmospheric entry by landers and rovers.

23 Predominant wavelengths were 3–14 km and amplitudes were generally 0.8%–2.5%.

24 Where static stability is large and positive, gravity waves grow efficiently. In other  
25 instances, static stability is not large and positive over a wide altitude range, and  
26 gravity wave amplitudes do not behave as neatly.

27 These observations of gravity waves in the middle atmosphere of Mars can be used  
28 to test gravity wave parameterizations in large-scale general circulation models and to  
29 investigate predictions for how gravity wave propagation and dissipation influence the  
30 circulation and thermal structure of the middle and upper atmosphere.

31 *Keywords:* Mars, planetary atmospheres, stellar occultation, gravity waves

## 32 1. INTRODUCTION

33 Internal gravity waves are atmospheric waves that propagate vertically upwards in fluid, stably  
34 stratified planetary atmospheres (Fritts & Alexander 2003; Yiğit & Medvedev 2015). They are com-  
35 mon features in such atmospheres. They are associated with the adiabatic displacement of air parcels  
36 that are restored to their original positions by buoyancy forces. Gravity waves are distinguished from  
37 physically-similar oscillations (e.g., Rossby waves, thermal tides) by their small horizontal scales  
38 (much less than a planetary radius) and short periods (much less than a planetary rotation period)  
39 (England et al. 2017). Gravity waves can be generated by flow over topography, convective processes,  
40 wind shear, weather fronts, and other sources (Fritts & Alexander 2003; Yiğit & Medvedev 2015).  
41 These sources are usually located at tropospheric altitudes but waves can be generated at higher  
42 altitudes by local convective instabilities.

43 Gravity waves are important for vertical coupling within a planetary atmosphere. Propagating  
44 gravity waves carry vertical fluxes of horizontal momentum and energy, but not mass. Conservation  
45 of energy dictates that, in the absence of dissipation, gravity wave amplitudes increase with increasing  
46 altitude as atmospheric mass density decreases. This trend is disrupted where waves break, dissipate,  
47 or saturate. Wave breaking or dissipation, the former term reserved for more violent amplitude

decrease, results in depositing momentum and energy into the local atmosphere in a narrow vertical altitude range. Saturation describes a wave whose amplitude neither increases nor decreases with altitude ([Fritts & Alexander 2003](#)).

This transport of momentum and energy from the lower atmosphere to higher altitudes influences the mean circulation and thermal structure of these higher altitude regions. Gravity waves can influence dynamics by slowing or reversing mean flows in the upper atmosphere. The adiabatic perturbations of the waves create local temperature fluctuations even in regions where the waves propagate stably. Where gravity waves dissipate and/or break, the deposition of energy may either increase or decrease atmospheric temperatures, depending on the local atmosphere conditions. Gravity waves also contribute to turbulent mixing of the atmosphere. Furthermore, gravity waves contribute to stochastic atmospheric variability in these higher altitude regions.

On Earth, gravity waves influence mesospheric circulation and associated winter polar warming, initiate sudden stratospheric warming events, and excite the quasi-biennial oscillation ([Fritts & Alexander 2003](#); [Yigit & Medvedev 2015](#)). On Mars, gravity waves affect middle atmospheric circulation and associated winter polar warming ([Barnes et al. 2017](#); [Gilli et al. 2020](#); [Heavens et al. 2020](#)). They may also create localized cold pockets that promote the condensation of CO<sub>2</sub> ice clouds ([Spiga et al. 2012a](#)). They can cause large density variations in the thermosphere which affect the homopause location. As these waves dissipate, they modify the background thermal structure of the atmosphere. In the mesosphere and thermosphere, the cooling effects of gravity waves are comparable to the effects of the primary radiative mechanism, infra-red radiation by CO<sub>2</sub> molecules ([Smith et al. 2017](#); [Gilli et al. 2020](#); [Heavens et al. 2020](#)). The effects of gravity waves appear to be more impactful on Mars than on Earth, modifying circulation and atmospheric structure significantly ([Gilli et al. 2020](#); [Heavens et al. 2020](#); [Gubenko et al. 2015](#)). This is consistent with Mars having significantly greater topographic variations than Earth and a lower Brunt-Väisälä (buoyancy) frequency on average. Moreover, gravity waves on Mars have been detected with larger amplitudes and broader spectra than on Earth ([Gubenko et al. 2015](#)).

Gravity waves on Mars that affect thermospheric conditions are generated in the lower atmosphere, but the dependences of gravity wave activity on latitude and time of day differ between the lower atmosphere and the thermosphere. Activity is greatest in the tropics in the lower atmosphere (Creasey et al. 2006a; Ando et al. 2012; Tellmann et al. 2013a; Heavens et al. 2020), but smallest in the tropics in the thermosphere (Creasey et al. 2006b; Fritts et al. 2006; Withers 2006; England et al. 2017; Yiğit et al. 2015; Vals et al. 2019; Terada et al. 2017). Gravity wave amplitudes are greatest on the cold nightside in the thermosphere (England et al. 2017). Relationships between gravity wave activity in the thermosphere and in the lower atmosphere are influenced by the propagation of gravity waves through the intervening middle atmosphere. Observations of gravity waves in the middle atmosphere can offer valuable insight into gravity wave propagation and dissipation, thereby contributing to improved understanding of how gravity waves affect the circulation and thermal structure of the middle and upper atmosphere. Yet observations of gravity waves in this critical middle atmosphere region are extremely rare.

Consequently, many important questions about the behavior of gravity waves in the middle atmosphere of Mars remain unresolved. What are the characteristic wavelengths of gravity waves in the middle atmosphere? What are the amplitudes of gravity waves in the middle atmosphere? How does gravity wave amplitude change with altitude in the middle atmosphere? What seasonal and diurnal variations impact the location, strength, and amplitudes of gravity waves?

In order to advance understanding of the role of gravity waves in the atmosphere of Mars, the aim of this report is to characterize small-scale structure in atmospheric profiles at middle atmospheric altitudes. This aim will be achieved by analysis and interpretation of two types of data: Earth-based observations of the occultation of the bright star  $\epsilon$  Geminorum by Mars in 1976 and entry profiles from Vikings 1 and 2, Pathfinder, Spirit, Opportunity, Phoenix, Curiosity, and InSight.

The structure of this article is as follows. Section 2 introduces gravity waves in the atmosphere of Mars. Section 3 introduces the stellar occultation method for measuring atmospheric profiles. Section 4 describes the 1976 occultation of  $\epsilon$  Geminorum by Mars. Section 5 describes how high-resolution atmospheric profiles were obtained from this occultation in a reanalysis of archival data. Section 6

assesses and validates these occultation profiles. Section 7 introduces the aerodynamic drag method for measuring atmospheric profiles during a spacecraft’s atmospheric entry. Section 8 characterizes the small-scale structure present in both types of atmospheric profile. Section 9 interprets the findings of Section 8. Section 10 discusses the behavior of gravity waves in the middle atmosphere of Mars. Section 11 presents the conclusions of this work.

## 2. GRAVITY WAVES IN THE ATMOSPHERE OF MARS

Gravity waves on Mars have primarily been observed via their effects on atmospheric density, pressure, and temperature profiles. Such profiles have been acquired by several different types of instrument, including radio occultations, infra-red limb sounders, ultraviolet stellar occultations, and *in situ* density measurements from orbiters and landers. Earth-based observations of stellar occultations can also provide such profiles.

Radio occultation observations provide vertical profiles of atmospheric density, pressure, and temperature between the surface and approximately 40 km altitude with vertical resolution of  $\sim$ 1 km. Creasey et al. (2006a) analyzed radio occultation profiles from Mars Global Surveyor. They used variations in temperature around the background state to determine the gravity wave potential energy per unit mass at 10–30 km altitude. In order to exclude long-wavelength thermal tides, they filtered these profiles to eliminate oscillations with vertical wavelengths greater than 10 km. They found that the potential energy was greatest in the tropics, notably over the Tharsis rise, with a maximum value on the order of  $10 \text{ J kg}^{-1}$ . Values outside the tropics were less than  $2 \text{ J kg}^{-1}$ . Ando et al. (2012) analyzed the same dataset to characterize the spectrum of gravity waves (i.e, dominant vertical wavelengths) at 3–32 km altitude. This analysis was sensitive to wavelengths in the range 2.5 km to 15 km. At wavelengths less than 8 km, they found that spectral power increased as wavelength increased. Furthermore, they found that the quantitative expression of this relationship, a power law, was consistent with terrestrial experience and theoretical expectations. At longer wavelengths, the spectral slope is markedly flatter. They attributed this to the presence of thermal tides. In addition, Ando et al. (2012) confirmed that gravity wave power is greatest in the tropics. Tellmann et al. (2013a) analyzed radio occultation profiles from Mars Express at 0–40 km altitude.

They also examined variations in temperature around the background state and filtered their results to eliminate oscillations with vertical wavelengths greater than 10 km, which were deemed to be influenced by thermal tides. Tellmann et al. (2013a) reported that wave amplitudes increased with increasing altitude, as expected. However, they found that this exponential growth ceased at  $\sim$ 33 km altitude, implying wave breaking at this altitude. They also noted that gravity wave activity was strongest around Tharsis. Here the amplitude of the temperature fluctuations reached  $\approx$ 6 K around 30–40 km altitude.

Infra-red limb sounding observations provide temperature-pressure profiles in the lower and middle atmosphere. MGS TES profiles from limb sounding generally extend from the surface to  $\sim$ 60 km altitude and the vertical resolution is approximately 10 km (Smith et al. 2001). Due to this coarse resolution, few gravity wave studies have been conducted with MGS TES profiles. Feofilov et al. (2012) were able to extend a small fraction of these profiles up to  $\sim$ 90 km. They noted strong profile-to-profile variability in their set of observations. They attributed this to gravity waves and reported that the root-mean-square of the temperature variability was 7 K at 60 km, 11 K at 70 km, 18 K at 80 km, and 25 K at 90 km. MRO MCS profiles generally extend from the surface to  $\sim$ 80 km altitude with vertical resolution of  $\sim$ 5 km. Wright (2012) analyzed temperature fluctuations in MCS profiles and filtered their results to eliminate oscillations with vertical wavelengths greater than 10 km, which were deemed to be influenced by thermal tides. They found that wave amplitude decreased with increasing altitude from tens of Kelvin at 200 Pa ( $\sim$ 5 km altitude) to  $<1$  K at 10 Pa ( $\sim$ 50 km altitude). Similarly, Creasey et al. (2006a) identified gravity waves decreasing in amplitude between 5 km and 35 km altitude using MGS radio occultation, which they attributed to saturation. Heavens et al. (2020) analyzed variations in MCS on-planet radiance observations, which they deemed to have been caused by gravity waves. This analysis was most sensitive to gravity waves with vertical wavelengths of 10 km or greater. Their use of on-planet (i.e., nadir or close to nadir) observations, as opposed to limb sounding observations, provided sensitivity to gravity waves with horizontal wavelengths of 10–30 km, unlike the hundreds of kilometers characteristics of limb sounding methods. They confirmed the association of gravity waves with topographic features and

155 also noted that the power of topographically-driven gravity waves is intermittent. They reported  
156 that gravity wave activity was increased by regional and global dust storms.

157 UV stellar occultation observations provide vertical profiles of atmospheric density, pressure, and  
158 temperature in the middle and upper atmosphere. Mars Express SPICAM profiles extend from 70  
159 km altitude to 130 km altitude with vertical resolution of  $\sim$ 3 km. The temperature uncertainty  
160 varies with altitude, but a characteristic value is 10 K. These profiles are generally smooth and show  
161 little indication of the presence of gravity waves ([Montmessin et al. 2006](#); [Quémerais et al. 2006](#);  
162 [Forget et al. 2009](#); [Withers et al. 2011](#)). MAVEN IUVS profiles have slightly smaller temperature  
163 uncertainties ( $\sim$ 5 K) than those of SPICAM, but show similarly little indications of gravity waves.  
164 Instead, longer-wavelength variations attributed to thermal tides are common ([Gröller et al. 2018](#)).

165 Earth-based observations of stellar occultations provide vertical profiles of atmospheric density,  
166 pressure, and temperature in the middle atmosphere. The 1976 occultation of  $\epsilon$  Geminorum by  
167 Mars provided two atmospheric profiles from  $\sim$ 50 km to  $\sim$ 90 km altitude with  $\sim$ 1 km vertical  
168 resolution, but small-scale variations in these profiles were not characterized in detail by the original  
169 experimenters ([Elliot et al. 1977b](#)).

170 *In situ* density measurements at thermospheric altitudes also display signatures of gravity waves.  
171 Aerobraking accelerometer observations have been analyzed by several authors. [Fritts et al. \(2006\)](#)  
172 found horizontal wavelengths of 20–200 km and density amplitudes of 5%–50%. [Creasey et al.](#)  
173 ([2006b](#)) found horizontal wavelengths of 100–300 km. They also noted that the amplitudes of density  
174 fluctuations were not appreciably greater in the tropics than at other latitudes. [Withers \(2006\)](#)  
175 found that the amplitudes of density fluctuations were smaller in the tropics than at other latitudes.  
176 This is in contrast to results at tropospheric altitudes that show greater gravity wave activity in  
177 the tropics. MAVEN neutral mass spectrometer (NGIMS) observations have also been analyzed by  
178 several authors. [Yiğit et al. \(2015\)](#) reported density variations of 20–40% at 180–220 km altitude.  
179 [England et al. \(2017\)](#) found that the amplitude of density fluctuations depended on species mass.  
180 Mass-dependent behavior of the effects of gravity waves was previously seen at Venus and Earth.  
181 These amplitudes were anti-correlated with the background atmospheric temperature, such that

variations were larger on the nightside than the dayside. Below 205 km, fluctuations in CO<sub>2</sub> density presented horizontal wavelengths on the order of 200 km and amplitudes of roughly 5%–25%. Terada et al. (2017) also reported density fluctuations of 10%–20% with amplitudes being anti-correlated with the background atmospheric temperature. Hence nightside amplitudes were greater than dayside amplitudes. Siddle et al. (2019) found density fluctuations of ∼10% and vertical wavelengths of 10–30 km. Amplitudes increased from the dayside to the nightside, as seen by England et al. (2017).

The entry, descent, and landing of spacecraft on the surface of Mars provide vertical profiles of atmospheric density, pressure, and temperature between ∼10 km and ∼120 km altitude with sub-km resolution. Magalhães et al. (1999) reported oscillations in temperature with vertical scales of ∼5 km and amplitudes of ∼2–3 K at 80–120 km altitude in the Pathfinder entry profile. Small-scale variations are present in similar profiles from Vikings 1 and 2, Spirit, Opportunity, Phoenix, Curiosity, and InSight (Seiff & Kirk 1976; Withers & Smith 2006; Withers & Catling 2010; Holstein-Rathlou et al. 2016; Banfield et al. 2020), but have not been characterized in detail.

In the lower atmosphere, gravity waves have been observed with km-scale vertical resolution by radio occultations. In the upper atmosphere, gravity waves have been observed with km-scale vertical resolution by in situ density measurements from aerobraking accelerometers and orbiting mass spectrometers. In the middle atmosphere, however, observations of gravity waves with km-scale vertical resolution are rare. Infra-red limb sounders like MGS TES and MRO MCS provide profiles with vertical resolution of 5–10 km. Ultraviolet stellar occultations from MEX SPICAM and MAVEN IUVS provide profiles with vertical resolution of ∼3 km, but temperature uncertainties of 5–10 K mask the small temperature fluctuations caused by gravity waves. Only a handful of Earth-based stellar occultations and atmospheric entry profiles have sampled middle atmosphere conditions with km-scale vertical resolution and sufficient accuracy to reveal gravity waves.

### 3. STELLAR OCCULTATIONS

The technique of stellar occultations has been used for over half a century to observe solar system atmospheres with high spatial resolution (Baum & Code 1953; Elliot & Olkin 1996).

208 As a solar system object with a fluid atmosphere passes across the line of sight from an observer  
209 (usually on Earth) to a star, the observed flux from the star is gradually reduced. The flux is  
210 impacted by three factors: atmospheric refraction, atmospheric lensing, and extinction by absorption  
211 of scattering. The time series of stellar flux from an occultation is called a light curve. Refraction  
212 sets the overall shape of the light curve, with significant contributions from lensing and extinction  
213 depending on conditions (Elliot & Young 1992; Chamberlain & Elliot 1997).

214 Immersion (also called “ingress”) is the beginning of the occultation, when the solar system object  
215 moves into the line of sight from the observer to the star. Emergence (also called “egress”) is the end  
216 of the occultation, when the solar system object moves out of the line of sight from the observer to  
217 the star. The central flash is a brief, yet sometimes intense, enhancement in flux in the middle of the  
218 occultation caused by simultaneous refraction around the limb of the solar system object as the star  
219 is nearly directly behind the object from the perspective of the observer. This is somewhat analogous  
220 to the “Einstein ring” effect in gravitational lensing. It only occurs when the chord of the star across  
221 the occulting object passes close to the centroid of the occulting disk. Its exact shape is determined  
222 by the atmospheric oblateness and orientation of the occultation geometry (Elliot & Olkin 1996).

223 “Occultations of stars by planetary atmospheres — observed from the vicinity of the Earth —  
224 probe the temperature, pressure, and number-density profiles of planetary atmospheres with a typical  
225 vertical resolution of a few kilometers. Because the main process causing the starlight to dim is the  
226 spreading of light rays through refraction by the atmosphere of the planet, this method detects all  
227 gases in the atmosphere. The technique is sensitive to an altitude interval of about five scale heights  
228 at the microbar pressure level, depending on the distance between the observer and occulting planet.  
229 For cases when the observer is near the center of the planetary shadow, focusing of the starlight by  
230 the occulting planet greatly enhances the stellar flux in the shadow plane and allows much deeper  
231 probing of the atmosphere than is possible from the main drop and recovery of the occultation light  
232 curve” (Elliot & Olkin 1996). The sensitivity of stellar occultation observations to atmospheric  
233 conditions around the microbar level enables them to probe middle atmospheric regions that are  
234 often challenging to observe by other methods.

The rate of change of flux during an occultation provides a direct indication of the scale height of the planetary atmosphere, although this is rather sensitive to the experimental calibration and background subtraction. Occultation light curves also provide the oblateness of a planetary atmosphere, either from multiple chords across an object or from analysis of the central flash. For the giant planets, this oblateness can be used to investigate zonal wind patterns.

#### 4. THE 1976 OCCULTATION OF $\epsilon$ GEMINORUM BY MARS

The 8 April 1976 occultation of  $\epsilon$  Geminorum, a relatively bright star (V-band magnitude of 3.1), by Mars was observed by groups at several locations around the United States and the Kuiper Airborne Observatory (KAO) (Elliot et al. 1977a,b; French & Elliot 1979; French & Taylor 1981; Hubbard 1982; Keenan & McNeil 1989). During the occultation, the KAO was 12.5 km above the Atlantic Ocean, several hundred miles east of North Carolina, USA, at 36°N, 290°E (Elliot et al. 1976). At 12.5 km altitude, the KAO 91 cm telescope observed roughly three times higher signal-to-noise than what a comparable instrument would have observed on the ground (Young 1967). This occultation was particularly noteworthy in that the group aboard the KAO reported the first central flash observed in a stellar occultation.

These observations were acquired at Ls=52° in Mars Year 12 (Clancy et al. 2000). The immersion profile sampled the atmosphere of Mars at 27°S, 29°E at a local solar time of 3.5 hours. The emersion profile sampled 28°N, 208°E at a local solar time of 15.5 hours. These profiles extended from ~50 km to ~90 km altitude, or pressure levels of 0.1–100 microbars. “The mean temperature is ~145 K, and the profiles exhibit wavelike structures with a peak-to-peak amplitude of 35 K and a vertical scale of about 20 km” (Elliot et al. 1977b). These long-wavelength fluctuations were interpreted as being caused by thermal tides. The results were broadly consistent with the Viking Lander 1 and 2 entry profiles that were obtained in July and September 1976, respectively (Seiff & Kirk 1976).

Data were observed with a 4 ms cadence on photomultiplier tubes. In the original analysis of these occultation light curves, the authors chose to bin the data by a factor of 25 to reduce computation time (Elliot et al. 1977b). This also resulted in a reduction of vertical resolution. Though the published results had a vertical resolution of 1–2 km, this was insufficient to resolve gravity waves because

262 subsequent points produced by the inversion process are highly correlated (see Section A). This  
263 means a vertical spacing between points of 1–2 km is insufficient to detect temperature perturbations  
264 of a size of similar magnitude.

265 The original atmospheric profiles obtained from the KAO observations have been lost. However,  
266 the raw data still exist.

267       5. REANALYSIS OF THE  $\epsilon$  GEMINORUM OCCULTATION

268           5.1. *Data Calibration*

269       The raw data from the observation are shown in Figure 1, which indicates a decreasing sensitivity  
270 of Channel 1 over time. Unfortunately, any calibration data obtained is undocumented and the  
271 instrument is long since destroyed, so we were unable to ascertain the cause of this baseline trend.  
272 Given that the trend is apparent only in one of the channels, we suspect without conclusive evidence,  
273 that it was the result of a saturation in that photomultiplier. Regardless of the cause, we fit the data  
274 away from occultation to a linear trend and subtract the baseline trend to correct for it. Quadratic  
275 and exponential fits were also tested but both converge to nearly linear fits. Therefore, for the rest  
276 of this analysis, we stick to the linear fit.

277       Following the same procedure as Elliot et al. (1977b), we normalize the three channels such that  
278 flux at upper baseline is assigned a value of 1.0 and flux during occultation is assigned a value of  
279 0.0. The upper baseline and occultation levels were assessed by taking the median of symmetric  
280 portions of the light curves, avoiding immersion, emersion, and the central flash. Figure 2 shows the  
281 normalized light curves of all three channels and Figure 3 highlights the immersion and emersion  
282 portions of the normalized light curves, showing finer detail.

283       The data were recorded in 4 ms integrations. As mentioned, the original work of Elliot et al. (1977b)  
284 used data binned to 0.1 s resolution, a factor of 25 decrease in temporal resolution. This choice was  
285 taken to limit the processing time of observations to match computational resources available. As  
286 those constraints are no longer true today, we use the full 4 ms resolution data, which ensures the  
287 best possible vertical resolution.

## 288        5.2. *Model Fitting*

289        The process of determination of atmospheric density, pressure, and temperature profiles from oc-  
290        cultation data requires some preparatory work. First, the location of the upper boundary of the  
291        resultant atmospheric profile must be selected. This requires the selection of the corresponding flux  
292        level, which involves a compromise between the desire to extend the profile as high as possible and the  
293        requirement that the diminution in flux caused by the atmosphere be discernible despite experimental  
294        noise. Second, the atmospheric conditions at this upper boundary must be specified.

295        To accomplish these requirements, an idealized atmospheric model is fitted to the data. We use  
296        the model fitting procedure of [Elliot & Young \(1992\)](#). We assume a clear atmosphere, thereby  
297        neglecting possible extinction by haze and dust. The Mars atmosphere is generally clear at this  
298        season ( $Ls=52^\circ$ ). Furthermore, dust and haze are rarely found on Mars at altitudes beyond a few  
299        km above the surface ([Montabone et al. 2015](#)). We assume an isothermal atmosphere. As the role of  
300        model fitting is to provide a boundary condition, an isothermal model is sufficient and standard (see  
301        e.g., [Pasachoff et al. 2016](#); [Bosh et al. 2015](#); [Person et al. 2008, 2013](#); [Person et al. 2019](#)). Furthermore,  
302        the middle atmosphere of Mars does not usually contain such exceptionally strong thermal gradients  
303        as to invalidate this assumption ([Smith et al. 2017](#)).

304        Fitting the immersion portion of the light curve yielded the isothermal scale height for that location.  
305        The typical approach is to fit the model to the high altitude portion of the light curve only. For  
306        example, [Elliot et al. \(1977b\)](#) fitted down to a flux level of 0.7. The full inversion then begins at  
307        that flux level. However, here we elected to fit the model to the entire immersion portion of the light  
308        curve and to begin the full inversion at the relatively large flux level of 0.9. The benefits of doing  
309        so are two-fold: one, we find a more reliable globally-averaged temperature measurement. Two, by  
310        starting at a higher flux level, we can perform a protracted search for wave activity over a larger  
311        vertical region of the atmosphere. The emersion portion of the light curve was fitted similarly.

312        We also fit an atmospheric model to the central flash portion of the light curve. As discussed  
313        in Section 3, deep stellar occultations have a central flash feature. This is caused by simultaneous  
314        refraction of starlight around the limb of the occulting body as the center of the occulting body

passes relatively close to the line of sight between the observer and the star. The KAO flight plan was designed to bring the observer-star line of sight as close to the center of Mars as possible. Hence the  $\epsilon$  Geminorum occultation has a strong central flash with two peaks that can be seen in Figure 2. The intensities of these two peaks are primarily determined by the impact parameter (the distance from the occultation chord to the centroid of the occultation shadow) and the atmospheric oblateness. We fit the [Elliot & Young \(1992\)](#) model to the central flash portion of the light curve. Note that [Elliot et al. \(1977b\)](#) did not have a robust model fitting approach to the central flash. Instead, they determined the impact parameter using forward modeling and evaluated their candidate fits by eye.

The immersion, emersion, and central flash model fits are shown in Figure 4 and the parameters resulting from the fits are outlined in Table 2. The immersion and emersion scale height values are consistent with previous findings ([Kieffer et al. 1992](#)). The atmospheric ellipticity value is roughly a factor of two lower than the solid body ellipticity of Mars. The goodness-of-fit parameters are acceptable.

The best model fit to the central flash may appear by eye to not fully fit the trends in the data. This is due to systematic uncertainties. For example, the model does not account for a dip in flux before the central flash, as can be seen at 1795 seconds in the middle panel of Figure 4. It is possible that this dip is due to atmospheric structure that the central flash model of [Elliot & Young \(1992\)](#) does not include and therefore the fit is worse than captured by the reported errors.

Another source of systematic error is that the central flash fitting relies on the fitting results to immersion and emersion. For instance, a small error in the value of occultation mid-time when fitting the immersion and emersion curves may be introduced due to photon noise. Though it hardly affects the fit of the limbs, this error applied to the central flash may cause the model to vary other parameters in an attempt to correct a slightly incorrect mid-time. The result is systematic uncertainties that are grossly underestimated by the random uncertainties reported in Table 2. A 10 km uncertainty on the impact parameter is more realistic, which results in an approximately 10 km uncertainty in altitude.

In an occultation taken today, these uncertainties would not be acceptable. Modern GPS and planetary ephemerides make it possible to astrometrically solve for the occultation geometry. The KAO position was recorded by inertial sensors during observations, which identified a 2 arcminute discrepancy in latitude and longitude upon landing (Elliot et al. 1977b). Furthermore, running modern ephemerides four decades back in time introduces difficult-to-calibrate uncertainties. Given these constraints, we accept the  $\sim 10$  km vertical uncertainty and reiterate that it does not materially impact the findings of this work. We express vertical altitude primarily in terms of pressure and otherwise only use relative altitude comparison.

### 5.3. *Inversion*

In this reanalysis, we follow the inversion procedure outlined in Elliot, Person, & Qu (2003), which is the seminal work on the modern approach to the French et al. (1978) inversion procedure used in the original work. The details of the inversion process are summarized in Appendix A. We assume the boundary conditions reported in Table 2. Note that the upper boundary conditions determined by model fitting (Section 5.2) were influenced by atmospheric properties above and below this boundary. While it is formally undesirable that atmospheric properties below the upper boundary influence the upper boundary conditions, the negative consequences of this are minor.

The inversion approach assumes that refracted light rays do not cross (Appendix A). A corollary of this is that all normalized flux values used in the inversion must be positive because a negative normalized flux value implies a degeneracy in parameter space that cannot be resolved with these observations alone. Some of the full-resolution normalized flux values are negative due to noise, which is resolved by binning data points as needed to ensure positive normalized flux values (Elliot et al. 2003).

If the inversion procedure encounters a negative normalized flux value as it advances downwards in altitude, it averages it with the requisite number of subsequent points to create a positive normalized flux value. The effect is the same as binning, but this method applies the minimum binning possible at each point rather than a consistent bin size everywhere, which preserves as much of the vertical resolution as possible.

368     The lower boundary of the atmospheric profile is set by noise. Inversion ends either when the  
369     binning becomes too large to perform analysis or when the measured flux values are dominated by  
370     photon noise and no longer represent real atmospheric structure. In our reanalysis, observations are  
371     limited to the middle Martian atmosphere in the pressure range  $0.1 \mu\text{bar} \lesssim p \lesssim 10 \mu\text{bar}$  (50 km  
372      $\lesssim z \lesssim 95$  km), where  $p$  is pressure. This approximately corresponds to the same altitude range of  
373     the original analysis.

## 374     6. RESULTS FROM REANALYSIS OF THE OCCULTATION OBSERVATIONS

### 375         6.1. *Issues of Altitude*

376     The primary data products of this work are two vertical profiles of number density, pressure, and  
377     temperature of the Martian middle atmosphere. Occultation profiles are formally determined in terms  
378     of radial distance (see Section 5.3). We converted our radial distances to altitude by subtracting the  
379     appropriate radius of the areoid (gravitational equipotential surface) produced by the Mars Orbiter  
380     Laser Altimeter (MOLA) experiment aboard the Mars Global Surveyor (MGS) spacecraft ([Lemoine et al. 2001](#)). At the latitudes and longitudes of the immersion and emersion profiles, the areoid  
381     radius is 3391.8 km and 3392.3 km, respectively. This reference areoid was not available to [Elliot et al. \(1977b\)](#), who instead converted radial distances to altitudes by subtracting  $3401 \pm 5$  km and  
382     3404  $\pm 7$  km, respectively, from their immersion and emersion radial distances.

385     Comparison of pressure-altitude profiles (not shown) from our reanalysis and the original results  
386     of [Elliot et al. \(1977b\)](#) revealed unexpected discrepancies. Pressure decreases roughly exponentially  
387     with increasing altitude. Yet our pressure-altitude profiles and those of [Elliot et al. \(1977b\)](#) were  
388     offset by approximately 10 km on both immersion and emersion.

389     As explained in Section 5.2, we expect a discrepancy of this order due to the systematic uncertainties  
390     of fitting a model to the central flash feature. The approximately 10 km uncertainty in the impact  
391     parameter translates to a similar uncertainty in the radial distances of each data point in the profile.  
392     Note that this source of error affects the absolute values of radial distance. It does not affect relative

radial distances or altitudes in a given profile. Our reanalysis and the analysis of Elliot et al. (1977b) adopted different values for the impact parameter, which leads to differences in radial distance.

We introduced additional information to resolve this discrepancy. The Mars Climate Database (MCD) (Millour et al. 2019) is a robust general circulation model benchmarked with *in situ* and remote sensing measurements from current and former missions to Mars. We compared pressure-altitude profiles from our reanalysis and from Elliot et al. (1977b) to relevant output from the MCD, then found the altitude adjustment necessary to bring each occultation profile into alignment with the relevant MCD profile.

We adjusted the nominal values of altitude in the immersion and emersion profiles of Elliot et al. (1977b) by 4 km and 7 km, respectively. Similarly, we adjusted the nominal values of altitudes in our immersion and emersion reanalysis profiles by 14 km and 15 km, respectively. Note that this adjustment does not affect temperature-pressure profiles (Section 6.2) or the wave analysis of subsequent sections.

## 6.2. Atmospheric Profiles

Figure 5 shows the immersion and emersion temperature-pressure profiles from the channel 2 and channel 3 light curve data. Close inspection of data from channel 1 reveals that it has significantly worse signal-to-noise than the other channels, so we neglect results from channel 1 in the remainder of this article.

Figure 5 also shows the versions of these profiles that were obtained in the original analysis of Elliot et al. (1977b). The numerical results have been lost, so we recovered these profiles from the published work using the `graphClick` software. Relevant figures in Elliot et al. (1977b) showed pressure as a function of altitude and temperature as a function of altitude, but not temperature as a function of pressure. We combined results recovered from these two representations to obtain the temperature-pressure profiles shown in Figure 5. Figure 5 also shows simulated atmospheric profiles from the MCD.

Figure 5 includes altitude as a secondary axis. As the corresponding pressure-altitude profiles for the five temperature-pressure profiles included in this figure are formally different, the altitude axis is approximate.

### 6.3. Validation of the Atmospheric Profiles

Our reanalysis profiles are generally similar to the original results of Elliot et al. (1977b). Mean temperatures are similar and large-scale structures are similar. Furthermore, the channel 2 and channel 3 immersion profiles are more self-consistent in our reanalysis than in Elliot et al. (1977b). Our emersion profiles are also more self-consistent than those of Elliot et al. (1977b). These outcomes are encouraging for the validity of the results of our reanalysis.

For immersion, the mean temperatures in the reanalysis profile and the MCD profile are consistent. Furthermore, the wavelengths and amplitudes of large-scale structure in temperature are also similar in the reanalysis profile and the MCD profile. In the reanalysis immersion profile, the characteristic wavelength is around 23 km and the characteristic peak-to-peak amplitude is around 30 K. In the MCD immersion profile, the corresponding values are 30 km and 25 K. Yet the phasing of temperature extrema are not particularly consistent between these two profiles. The reanalysis immersion profile has a temperature maximum of 162 K at  $0.72 \mu\text{bar}$ , whereas the MCD immersion profile has a temperature maximum of 161 K at  $2.0 \mu\text{bar}$ . The reanalysis immersion profile has a temperature minimum of 128 K at  $2.3 \mu\text{bar}$ , whereas the MCD has a temperature minimum of 136 K at  $12.3 \mu\text{bar}$  (below the bottom of Figure 5a). For emersion, the reanalysis profile agrees well with the corresponding MCD profile.

Overall, the reanalysis profiles are more self-consistent than the original profiles. Moreover, the reanalysis profiles are at least as consistent with the MCD profiles as the original profiles are. We conclude that the reanalysis profiles are acceptable for scientific interpretation.

#### 6.4. Distinctive Features of the Atmospheric Profiles

442 Mean temperatures are similar in the immersion and emersion profiles, approximately 150 K. Long-  
443 wavelength structure is present in both profiles. Vertical wavelengths are similar in both profiles,

( $\sim$ 20–25 km), but the peak-to-peak amplitude is greater in the immersion profile ( $\sim$ 30 K) than in the emersion profile ( $\sim$ 10 K). We concur with the assessment of the original observers that this long-wavelength structure is likely caused by thermal tides. Short-wavelength structure is also present in both profiles at a vertical wavelength of roughly 5 km. This is evident in, for example, the channel 2 emersion profile around 1  $\mu$ bar pressure (Figure 5).

As outlined in Section 2, these fluctuations are likely to be caused by gravity waves. They are not apparent to the naked eye in the original profiles. As the original profiles averaged the raw 4 ms data to 0.1 seconds, their vertical resolution is 1 km. As detailed in Section 4, 1 km vertical resolution in an occultation is typically insufficient to observe variations on the same order of magnitude.

As averaging was not required for the reanalysis profiles, we produce better vertical resolution of 0.01–0.1 km. This improvement in vertical resolution renders small-scale structure much more visible.

## 7. ENTRY PROFILES

Spacecraft enter atmospheres at speeds comparable to orbital speeds. Typical values are several kilometers per second, much greater than the speed of sound in planetary atmospheres (Houghton 2002). A spacecraft entering a planetary atmosphere at hypersonic speed decelerates due to atmospheric drag (Withers et al. 2003b). Momentum is transferred from the spacecraft to the atmosphere at a rate which can be estimated from the principle of conservation of momentum. The spacecraft of area  $A$  traveling at speed  $v$  sweeps through a volume  $Av\Delta t$  of atmospheric gas in time  $\Delta t$ . The mass of this amount of air is  $\rho Av\Delta t$ , where  $\rho$  is the local atmospheric mass density. Assuming that this amount of air is accelerated to the same speed as the spacecraft, its momentum is  $\rho Av^2\Delta t$ . The momentum gained by the atmosphere per unit time, equivalent to that lost by the spacecraft per unit time, is  $\rho Av^2$ . This is the aerodynamic force acting on the spacecraft, a result which is surprisingly accurate (Withers 2013). Even with sophisticated numerical simulations, the aerodynamic force on a spacecraft is typically within a few tens of percent of  $\rho Av^2$ . Neglecting the effects of gravity on the spacecraft (mass  $m$ ), which is reasonable in the initial stages of atmospheric entry, gives the drag

469 equation.

$$m \frac{dv}{dt} = -\rho A v^2 \frac{C}{2} \quad (1)$$

470 The dimensionless coefficient  $C$ , which is close to 2, accounts for small deviations from the idealized  
471 situation outlined here.

472 Given knowledge of a spacecraft's entry trajectory, the profile of atmospheric density along this  
473 trajectory can be found using Equation 1. The trajectory is reconstructed using *in situ* measurements  
474 of acceleration during entry and the initial state of the spacecraft at the top of the atmosphere.  
475 Reliable density measurements are obtained over a wide vertical range. The upper boundary, which  
476 is generally at thermospheric altitudes, is set by instrumental sensitivity. The lower boundary, which  
477 is generally deep in the troposphere, is the altitude of parachute deployment. Spacecraft dynamics  
478 under a parachute are complex, which makes it difficult to determine atmospheric density from  
479 acceleration measurements.

480 Atmospheric entry profiles at Mars have been acquired by Viking Landers 1 and 2, Pathfinder,  
481 Spirit, Opportunity, Phoenix, Curiosity, and InSight (Seiff & Kirk 1976; Magalhães et al. 1999;  
482 Withers & Smith 2006; Withers & Catling 2010; Holstein-Rathlou et al. 2016; Banfield et al. 2020).  
483 Typical vertical extent is 10–100 km. We analyze small-scale structure in all atmospheric profiles  
484 from the descent of these landers. The locations, seasons, and times of day of these entry profiles are  
485 listed in Table 1.

## 486 8. OBSERVATIONS OF SMALL-SCALE STRUCTURE IN THE MIDDLE ATMOSPHERE

### 487 8.1. Approach

488 We use a four-step procedure to characterize the waves present in the four occultation reanalysis  
489 profiles (two channels for each immersion and emersion) and the eight entry profiles. This procedure  
490 focuses on perturbations in the density profile, as density is the atmospheric property most closely  
491 connected to the flux (occultation) and acceleration (entry) measurements directly observed.

492 Our procedure is as follows.

(1) *Density excursion.* Following Person et al. (2008), we isolate density departures from an idealized, isothermal atmosphere. We fit observed number density ( $n$ ) to the isothermal model

$$\bar{n} = n_0 e^{(z-z_0)/H}, \quad (2)$$

where  $n_0$  is a reference density,  $z_0$  is a reference altitude, and  $H$  is the pressure scale height. The density excursion is given  $n/\bar{n}$ .

(2) *High-pass filter.* The features of greatest interest are those of short vertical wavelength, not the larger-scale thermal tides. We therefore use a high-pass filter to isolate the shorter wavelength scales. Specifically, we employ the Savitzky-Golay filter, often called “savgol,” which fits a polynomial of order  $M$  to a window of size  $N$  at each point in the data (Savitzky & Golay 1964). In our experiments,  $M = 2$  had the greatest success removing artifacts and values of  $N$  in the range [3, 40] km were explored. We calculate a savgol filter value ( $SG$ ) for each density excursion and subtract it off, leaving behind an isolated waveform of interest.

In our experiments, any individual choice of window size  $N$  has certain limitations. For example, a window size of 5 km will filter out most longer wavelengths, creating the perception that those wavelengths are not present in the data. This is desirable in the case of thermal tides, which we want to distinguish clearly from small-scale perturbations. But in identifying the relative strengths of 5 and 10 km waves, for example, we do not wish for the user-defined filter window to significantly impact our findings. Therefore, for each of the profiles, we performed many savgol filters with window size  $N$  in the range [3, 40] km.

(3) *Amplitude Spectrum.* We find the amplitudes of harmonic contributions present in each profile from the Fourier transform of the filtered wave. As mentioned above, we choose to savgol filter each profile at many different filter window sizes, each of which produces an amplitude spectrum. We compiled the results of these spectra into contour plots, which show filter window versus wavelength. The contour levels indicate amplitudes. The plots are shown in Section 8.2.

As mentioned in Section 4, numerical inversion of an individual flux measurement in an occultation light curve is highly dependent on the previous point. Therefore, inversion has the potential to create

waves out of smooth light curves with random noise. We tested this by using a control set of idealized, isothermal light curves with the same noise profile as the real occultation data. We inverted and processed these light curves and detected the distribution of peak amplitudes for each savgol filter window used on the real data. The resulting distributions are skew-normal, and are used to calibrate confidence intervals for the stellar occultation amplitude spectra shown in Section 8.2.

(4) *Amplitude Growth.* We look for wave amplitude variations that follow gravity wave theory (Mueller-Wodarg et al. 2008) and compare with static stability.

Under stable atmospheric conditions, waves typically grow in amplitude as they propagate vertically because the decreasing atmospheric density requires greater amplitude to satisfy conservation of energy flux (Holton 2013). For each extracted wave form, we assessed the dependence of wave amplitude on altitude by identifying the wave peaks and finding the corresponding peak-to-peak amplitude values. We look for amplitude growth following the pattern  $A \propto n^{-(1/2)}$  (Mueller-Wodarg et al. 2008), where  $A$  is the filtered wave amplitude and  $n$  is number density.

Wave propagation is influenced by the atmospheric static stability. Static stability is defined as the difference between the dry adiabatic lapse rate  $\Gamma_d$  and the observed lapse rate  $\Gamma$ , which can be written

$$\Gamma_d - \Gamma = \frac{g}{c_p} + \frac{\partial T}{\partial z} \quad (3)$$

where  $c_p$  is the specific heat at constant pressure of the atmosphere ( $850 \text{ J kg}^{-1} \text{ K}^{-1}$ ; Magalhães et al. (1999)),  $g$  is the gravitational acceleration, and  $T$  is temperature (Holton 2013). A value of static stability near or below zero indicates regions of the atmosphere where the observed adiabatic lapse rate exceeds the limit of convective stability. It is held that convection quickly reduces the lapse rate to restore equilibrium, meaning that wave transport is likely not stable in this region and wave breaking might occur. We compare wave activity to static stability for each of the profiles.

Wave activity is further illustrated if we represent the filtered density excursion by a simple model:

$$1 + c_1 n(z)^{-\frac{1}{2}} \sin \left[ \left( \frac{2\pi z}{c_2} \right) - c_3 \right] \quad (4)$$

539 where  $c_1$ ,  $c_2$ , and  $c_3$  are parameters determined by approximately matching the model to the filtered  
 540 density excursion.  $c_1$  scales the width of the envelope of amplitude growth,  $c_2$  is the wavelength,  
 541 determined by the amplitude spectrum, and  $c_3$  determines the phase of the sine curve to align with  
 542 the observed wave.

## 543 8.2. Stellar Occultation Wave Results

544 Figures 6, 7, 8, and 9 are each four-panel plots showing density excursion, savgol filtered waves,  
 545 peak-to-peak amplitude, and static stability of emersion channels 2 and 3 and immersion channels  
 546 2 and 3, respectively. Here we display the results of a 10 km savgol filter window, the reasoning  
 547 for which is given below. A visual inspection of the c panels in each of the figures leads to the  
 548 conclusion that the emersion channel 2 data (Figure 6c) most closely follows the trend of wave  
 549 growth. Specifically, wave growth is consistent between 65 and 95 km, below which a pattern of  
 550 decreasing amplitude might indicate wave saturation or breaking. This interpretation of Figure 6c is  
 551 corroborated by Figure 6d, which shows a high static stability between 65 and 95 km, bookended by  
 552 low static stability.

553 The immersion profiles shown in Figures 8d and 9d show some regions of high static stability, but  
 554 frequent dips toward zero support the finding that those waves do not indicate amplitude growth. De-  
 555 spite this, Figures 8b and 9b do show narrow regions where waves are stable, even some of particularly  
 556 large amplitude.

557 As detailed in Section 8.1, Figure 10 shows the contour plot of amplitude spectra for every savgol  
 558 filter window of 3–40 km. Colored contours indicate amplitudes as a function of wavelength (y-  
 559 axis) for a given filter window (x-axis). The white contour lines indicate confidence intervals from  
 560 control data. We indicate amplitudes at each savgol window size that are confident to the 95% and  
 561 99.99% level based on the distribution of amplitude peaks from the control data. For instance, a 1%  
 562 amplitude wave is a highly significant ( $> 99.99\%$ ) when using a 10 km filter window. The same 1%  
 563 amplitude is not significant when using a 30 km filter window. This underscores the motivation of  
 564 using many filter windows.

Having both amplitudes and significances in Figure 10 enables us to hone in on the features of greatest interest. The large, highly significant, yellow features in the upper right-hand corner of each plot are the thermal tides. They are of much greater amplitude in the immersion data. Features of wavelength 8–12 km appear in all four profiles at high confidence as well, with amplitudes in the range of 1.4–3%. We also see features of wavelength 4–6 km with amplitudes in the range 0.5–1%. These latter two groups of features are of greatest interest because they exhibit wavelengths and amplitudes consistent with gravity wave features in the middle atmosphere of Mars.

In particular, the 4–6 km features would represent smaller wavelengths than have been detected previously if confirmed. Because these features are best detected with a savgol filter window of 10 km, we used that particular window size in Figures 6, 7, 8, and 9. Prior works referenced in Section 2 also chose to filter out perturbations with wavelengths longer than about 10 km. Tellmann et al. (2013b) used a 10 km vertical wavelength filter to remove tidal modes and Wright (2012) performed a similar filtering.

In Figure 11, we show the amplitude spectrum with the 10 km filter, essentially a cut at  $x = 10$  km in Figure 10. All four profiles show 4–6 km wavelength modes with significance exceeding 95% confidence, with two of them exceeding 99.99% confidence. Furthermore, the emersion channel 2 profile in Figure 10c is dominated by one wave mode more than any other, which is likely why that profile has the clearest indication of wave amplitude growth in Figure 6c.

We fit the gravity wave model (Equation 4) to the filtered emersion channel 2 profile (Figure 6b), finding the best fit with  $c_1 = 2.3 \times 10^7 \text{ m}^{-\frac{3}{2}}$ ,  $c_2 = 5.2 \text{ km}$ , and  $c_3 = 1.3 \text{ radians}$ . Figure 12 shows the model overplotted on the filtered profile. The model and observations agree well between 65 km and 95 km altitude, where the atmosphere is most stable for gravity wave propagation.

Overall, we find waves of wavelength 4–6 km and 8–12 km in the middle atmosphere of Mars from stellar occultation profiles that are consistent with gravity wave activity.

### 8.3. Entry Profile Wave Results

We produced plots showing density excursion, savgol filtered waves, peak-to-peak amplitude, and static stability for the entry profiles in the same manner as for the occultations. For the entry profiles we display the results of the 20 km savgol filter window, the reasoning for which is offered below.

Figure 13 shows the Viking 1 entry results. Figure 13b indicates varied wave activity, which in Figure 13c shows a limited agreement with the wave growth model below 60 km. Above 60 km there is a narrow region of wave dissipation coinciding with static stability below zero in Figure 13d. Above about 70 km, wave activity is again high and only shows potential dissipation above 100 km. The generally low static stability in Figure 13d might limit wave growth.

Figure 14 shows the Viking 2 entry results. Figure 14b shows lots of wave activity but Figure 14c indicates it does not follow the theoretical wave growth pattern. Figure 14d indicates regions of negative stability at 50 km and 100 km, but where stability is higher in the middle atmosphere, the highest amplitude waves are found.

Figure 15 shows the Pathfinder entry results. Figure 15b shows a steady wave pattern throughout, interrupted by two large wave trains between 60 and 95 km in altitude. Figure 15c indicates each of these wave trains follows the predicted wave growth pattern before breaking at 80 and 95 km. Figure 15d shows static stability is often low but does not dip below zero considerably in the middle atmosphere, consistent with each wave train briefly growing.

Figure 16 shows the Spirit entry results. Figure 16b depicts a visibly growing wave structure, which Figure 16c demonstrates follows the wave growth trend throughout the atmosphere. Figure 16d indicates high stability at all altitudes except those above 100 km, bolstering the case for a propagating wave in this profile.

Figure 17 shows the Opportunity entry results. Figure 17b is not as clear as Figure 16b but Figure 17c shows a global trend consistent with wave amplitude growth. Figure 17d indicates, as with Spirit, that the atmosphere is statically stable at all altitudes but those above 100 km.

Figure 18 shows the Phoenix entry results. Figure 18c identifies that amplitude growth follows a wave pattern from the bottom of the profile up to about 62 km, where the wave amplitude decreases. Figure 18d shows static stability greater than zero for all altitudes below 80 km, indicating the

617 amplitude decrease at 65 km is more likely to be wave saturation or dissipation than breaking. The  
618 difference between dissipation and breaking can be exemplified by comparing this figure to Figure  
619 15c at 95 km.

620 Figure 19 shows the Curiosity entry results. Figure 19c shows a weak growth pattern up to about  
621 60 km with another, briefer, wave growth pattern from 70 km to about 90 km. Figure 19d shows a  
622 decrease in static stability below zero at about 63 km, which coincides with saturation in the lower  
623 wave pattern. Static stability jumps up again above 80 km, coinciding with the upper wave pattern.

624 Figure 20 shows the InSight entry results. A starkly visible wave train in Figure 20b extends from  
625 60 km to 100 km at the top of the profile, with a maximum amplitude, as indicated in Figure 20c,  
626 at 75 km. Figure 20c indicates expected wave growth from the bottom of the profile up to about 75  
627 km. Figure 20d shows static stability significantly greater than zero for the entirety of the profile,  
628 dropping lowest at about 65 km, which might precipitate the wave train dissipation above 75 km.  
629 Like Figure 18, this pattern is more likely to be wave dissipation than breaking.

630 Figure 21 shows the amplitude spectra contour plots for the entry profiles in the same manner as  
631 Figure 10 for the occultations. Upon inspection of the contour plots, we see that the features of 20–30  
632 km wavelength that only appear with larger filter windows are likely thermal tides. Regardless of  
633 their exact nature, they are not within the scope of this work and we therefore focus on the features  
634 of 9–14 km that appear with strong regularity. A 20 km filter window does a good job removing the  
635 large waves while keeping the 9–14 km features, which is our motivation for displaying the four-panel  
636 plots above with that filter.

637 Figure 22 shows the amplitude spectra of the entry profiles for the 20 km savgol filter window.  
638 Here we can see the 9–14 km features appear across all the profiles, ranging in amplitudes 0.8–2.6%.  
639 Some profiles, e.g., Spirit, show two-peaked features and others, e.g., Pathfinder, show single-peaked  
640 features.

#### 641 8.4. *Comparison of Primary Wave Findings*

642 The wavelengths, peak amplitudes, and confidences of all waves identified in the amplitude spectrum  
643 contours (Figures 10 and 21) are given in Table 3. From the occultation profiles, wave species are

644 included only if they exceeded the 95% confidence and have wavelengths between 3 and 20 km.  
 645 From the entry profiles, wave species are included only if they exceed amplitude of 0.5% and have  
 646 wavelengths between 3 and 20 km.

647 Figures 10 and 21 and Table 3 reveal common attributes between the occultation and entry profiles.  
 648 Wavelengths in the range 9–14 km are detected across many profiles, with amplitudes predominantly  
 649 1%–2.5%. Gravity waves within this range of wavelengths are among the most common detected in  
 650 the Martian atmosphere (Tellmann et al. 2013a; Siddle et al. 2019).

651 These results additionally reveal contrast between the occultation and entry profiles. Occulta-  
 652 tion profiles reveal waves of shorter wavelength (3–6 km) and entry profiles reveal waves of longer  
 653 wavelength (16–20 km).

## 654 9. INTERPRETATION

655 Short-wavelength fluctuations comparable to those discussed in Section 8 have been seen throughout  
 656 the Mars atmosphere by a variety of limb sounding instruments. They have generally been interpreted  
 657 as gravity waves.

658 Numerous types of internal waves can exist in the atmosphere of Mars (Yigit & Medvedev 2015).  
 659 We consider acoustic waves, internal gravity waves, inertia-gravity waves, Rossby waves, and tides.  
 660 (Andrews et al. 1987; French & Gierasch 1974).

661 Acoustic waves satisfy  $\omega \gg f$ , where  $\omega$  is the angular frequency of the wave,  $f$  is the Coriolis  
 662 parameter,  $f = 2\Omega|\sin\phi|$ ,  $\Omega$  is the rotation rate of the planet, and  $\phi$  is latitude. For the vertical  
 663 wavelength of 3–6 km required by Section 8.2, their horizontal wavelength would be less than 10  
 664 km, much shorter than the path length of starlight through the atmosphere of Mars. Such waves  
 665 cannot be responsible for coherent vertical structure in the atmospheric profile obtained from a stellar  
 666 occultation.

667 Internal gravity and inertia-gravity waves are similar. Both satisfy  $f < \omega < N$ , where  $N$  is the  
 668 Brunt-Väisälä or buoyancy frequency. This is defined as:

$$669 N^2 = \frac{-g}{\rho_0} \frac{\partial \rho}{\partial z}. \quad (5)$$

669 For the vertical wavelength of 3–6 km required by Section 8.2, their horizontal wavelength is comparable  
670 to the path length of starlight through the atmosphere of Mars. Such waves may be responsible  
671 for coherent vertical structure in the atmospheric profile obtained from a stellar occultation.

672 Rossby waves satisfy  $\omega \ll f$ . For the vertical wavelength of 3–6 km required by Section 8.2,  
673 they have horizontal wavelengths many times greater than the path length of starlight through the  
674 atmosphere of Mars. Such waves may be responsible for coherent vertical structure in the atmospheric  
675 profile obtained from a stellar occultation.

676 Tidal modes with the vertical wavelength of 3–6 km required by Section 8 do not propagate efficiently  
677 to the middle atmosphere of Mars (Withers et al. 2003a). Such waves cannot be responsible  
678 for coherent vertical structure in the atmospheric profile obtained from a stellar occultation.

679 We exclude Rossby waves from consideration, despite their long horizontal wavelength, because  
680 general circulation models indicate that Rossby waves on Mars would be confined to the very lowest  
681 regions of the atmosphere due to topographic forcing and dissipative effects (Fazel-Rastgar 2019).  
682 That leaves internal gravity waves and inertia-gravity waves as possible causes of the observed short-  
683 wavelength fluctuations.

684 Internal gravity waves are instances of inertia-gravity waves in which the effects of planetary rotation  
685 are small. This is equivalent to the Coriolis parameter in the dispersion relation being negligible  
686 (Andrews et al. 1987; French & Gierasch 1974; Yiğit & Medvedev 2015). For the short vertical  
687 wavelength relevant here, effects of planetary rotation are negligible.

688 Furthermore, numerical models of the mesosphere of Mars can reproduce gravity waves with features  
689 similar to those reported here. Spiga et al. (2012b) produced  $\sim 10$  km vertical wavelength gravity  
690 waves throughout the atmosphere (10 - 110 km altitude). Parish et al. (2009) produced gravity waves  
691 with 12 km vertical wavelength at about 25 km altitude.

692 We therefore concur with the widespread conclusion that short-wavelength fluctuations in Mars  
693 atmospheric profiles are caused by gravity waves. The species of 3–14 km wavelength that dominate  
694 detections in Table 3 align with previous detections and theoretical studies. The few detections  
695 of perturbations with longer wavelengths might be attributable to other sources. Regardless, the

overlap in detections between the stellar occultations and spacecraft entry profiles corroborates the interpretation of these perturbations as caused by gravity waves.

## 10. DISCUSSION

In section 1, we raised questions about gravity waves in the middle Martian atmosphere, the answers to which would significantly aid efforts to understand the critical middle atmospheric region and draw connections between upper and lower atmospheric dynamics. Here we answer these questions based on the findings in this work.

*What are the characteristic vertical wavelengths of gravity waves in the middle atmosphere?*

From re-analyzing of the 1976 Mars occultation of  $\epsilon$  Geminorum and analyzing the entry profiles of eight spacecraft, we find gravity waves predominantly with vertical wavelengths 3–14 km. See Table 3 for the breakdown of which wavelengths were detected from which data source.

*What are the amplitudes of gravity waves in the middle atmosphere?*

From producing amplitude spectra, we find amplitudes of dominant wavelengths in the middle atmosphere mostly fall in the range 0.8%–2.5%. A close inspection of Figures 6, 7, 8, 9, 13, 14, 15, 16, 17, 18, 19, and 20 reveals that in regions of the atmosphere most conducive to wave growth (positive static stability), amplitudes grow as large as 5% before saturating, dissipating, or breaking. See Table 3 for the summary of wave amplitudes from each data source.

*What regions in the Martian atmosphere are most conducive to gravity wave propagation? How does gravity wave amplitude change with altitude in the middle atmosphere?*

Within both the entry profiles and the occultation profiles, we can identify regions of the middle atmosphere more and less conducive to wave propagation. For example, Figure 6 (occultation emersion) indicates wave growth from 65 km to 90 km, where wave amplitude grows from 0.2% to 1%. Static stability remains far above zero for that altitude range. The Spirit results in Figure 16 show a growing wave from 60 km to 110 km, with amplitude growing from 1% to 5%. Static stability is far above zero for all but the highest altitudes in that range.

Other entry profiles indicate a different pattern of atmospheric stability. For example, the Phoenix profile in Figure 18 indicates significant wave growth from 30 km to 62 km, with amplitude growing

from 1% to 5%, but above 62 km, no clear wave growth is detected. Static stability corroborates this finding. In this case, with notable similarities to Pathfinder (Figure 15) and InSight (Figure 20), we see wave dissipation in an atmospheric region less conducive to wave propagation. In the case of InSight, this dissipation occurs at much higher altitudes, where effects such as molecular viscosity and radiative damping have been shown to have significant effect on wave patterns (Eckermann et al. 2011). The immersion occultation profiles show similar characteristics, with narrow vertical bands of stability, flanked by wave saturation and/or breaking.

We see that in regions of greater-than-zero stability, gravity wave amplitude follows the growth trend  $A \propto n^{-1/2}$ . In regions where stability barely dips below zero, e.g., Curiosity (Figure 19) at 62 km, wave growth patterns are disrupted. Moreover, in regions where static stability remains close to or repeatedly dips below zero, e.g., Viking 2 and Pathfinder (Figures 14 and 15), no global wave growth patterns can be established and wave growth is frequently interrupted. Both Viking profiles are curious in this manner because both amplitude spectra (Figures 22a and 22b) indicate a clear presence of waves that aligns with a visual inspection of the extracted waveforms (Figures 13b and 14b), but no global wave growth pattern is present (Figures 13c and 13c). The immersion channel 2 profile in Figure 8 has a region of stable wave growth following the amplitude trend only above 80 km.

This idealized wave growth pattern can only be expected for a quiescent atmosphere with positive static stability. Where these conditions are met globally, e.g., occultation emersion (Figure 6) and Spirit (Figure 16), we can expect gravity wave propagation throughout. Profiles in which these conditions are met only in narrow vertical ranges, e.g., occultation immersion (Figure 8), Phoenix (Figure 18), and Pathfinder 15, or not at all, e.g., Viking 2 (Figure 14), do not by default indicate a lack of gravity wave activity.

*What seasonal, diurnal, and latitudinal patterns in gravity wave activity exist?*

We explored amplitude and wavelength patterns with season, time of day, and latitude for all occultation and entry profiles and found no identifiable trends. We therefore reiterate the long-held finding that gravity wave activity is nearly universal on Mars.

## 750 11. CONCLUSIONS

751 Gravity waves are ubiquitous in the atmosphere of Mars. They have been studied extensively in  
752 the lower and upper atmosphere, but not in the middle atmosphere. Suitable atmospheric profiles  
753 that sample the middle atmosphere with good vertical resolution are rare: a ground-based stellar  
754 occultation from 1976 that yielded immersion and emersion profiles on opposite sides of the planet,  
755 plus eight profiles measured during atmospheric entry by landers and rovers.

756 This analysis of those observations has characterized the wavelengths and amplitudes of gravity  
757 waves in the middle atmosphere. Predominant wavelengths were 3–14 km and amplitudes were  
758 generally 0.8%–2.5%. Where static stability is large and positive, gravity waves grow efficiently. For  
759 the entry of the Spirit rover, for example, gravity wave amplitude grows from 1% at 60 km to 5% at  
760 110 km in accordance with the dependence on atmospheric density expected from idealized theoretical  
761 calculations. In other instances, static stability is not large and positive over a wide altitude range,  
762 and gravity wave amplitudes do not behave as neatly.

763 These observations of gravity waves in the middle atmosphere of Mars can be used to test gravity  
764 wave parameterizations in large-scale general circulation models and to investigate predictions for  
765 how gravity wave propagation and dissipation influence the circulation and thermal structure of the  
766 middle and upper atmosphere.

## ACKNOWLEDGMENTS

We acknowledge the work of the late Prof. James Elliot in taking these observations and performing the original analysis.

## APPENDIX

## 768 A. INVERSION PROCESS

769 Inversion of stellar occultation observations requires a number of assumptions, the most significant  
770 of which are as follows.

- 771 1. Atmospheric variation is a function of altitude only, implying uniformity across the planet at  
772 each altitude level.
- 773 2. Atmospheric composition is uniform.
- 774 3. The atmosphere is in hydrostatic equilibrium.
- 775 4. Extinction is negligible compared to refraction.
- 776 5. Bending angles due to refraction are small.
- 777 6. Planetary altitudes probed in immersion and emersion vary monotonically, *i.e.*, there is no ray  
778 crossing.
- 779 7. The Martian atmosphere is clear during these observation, *i.e.*, without dust or haze. (See  
780 Section 5.2.)

781 On small bodies with atmospheres significantly less than the terrestrial atmosphere, these assump-  
782 tions hold reasonably well. The original work of Elliot et al. (1977b) had one additional assumption,  
783 no longer required here, that the atmospheric scale height  $H$  is much less than the radius of Mars  
784 (Wasserman & Veverka 1973; French et al. 1978).

785 Figure 23 shows the geometry of atmospheric refraction that is solved by inversion. Figure 24 is  
786 a flowchart showing the steps of inversion from the normalized flux light curve  $\phi(t)$  to atmospheric  
787 properties. The other starting parameter is  $y(t)$ , where  $y$  is the distance of the observer relative to a  
788 reference point (usually defined at some arbitrary time before occultation). Values of  $y$  are calculated  
789 from the impact parameter ( $22.12 \pm 0.38$  km) and event velocity (21.9 km/s).

790 Given  $y(t)$  and  $\phi(t)$  it is possible to calculate the flux as a position series  $\phi(y)$ . The distance  
791 from the center of the occulting body corresponding to each flux measurement  $r(y)$  is calculated  
792 from  $y$  values given the distance between the observer and occulting body  $D$ , which is determined

by ephemerides of Mars provided by JPL HORIZONS (<http://ssd.jpl.nasa.gov/?horizons>).  $r(y)$  is solved using

$$r(y) = \left\{ y^2 + 2 \int_y^\infty [1 - \phi(y')] y' dy' \right\}^{1/2} \quad (\text{A1})$$

The bending angle  $\theta(r)$ , shown in Figure 23 is determined using  $r(y)$  and  $D$  by assuming the small angle approximation:

$$\theta(r) = \frac{y(r)}{D} \quad (\text{A2})$$

$\theta(r)$  is related to atmospheric index of refraction  $N(r)$  by the equation

$$\theta(r) = \int_{-\infty}^\infty \frac{r}{r'} \frac{d}{dr'} \ln N(r') dx \quad (\text{A3})$$

where  $x$  is defined by the geometry of Figure 23 as  $x^2 = r'^2 - r^2$ .  $r'$  is a variable of integration that iterates between 0 and  $r$  for each atmospheric shell of radius  $r$ . Refractivity  $\nu(r)$  is preferred to index of refraction  $N(r)$  and is related by

$$N(r) = 1 + \nu(r) \quad (\text{A4})$$

Equation A3 can be rearranged to solve for  $N(r)$  by using an Abel transform (Abel 1826), which gives, using Equation A4

$$\nu(r) = -\frac{1}{\pi} \int_r^\infty \frac{\theta(r')}{\sqrt{r'^2 - r^2}} dr' \quad (\text{A5})$$

invoking the assumption  $\nu \ll 1$ . This is the critical step of inversion that amounts to “unpeeling” the atmosphere to determine the effect of the gas at each layer on the starlight passing through.

Number density  $n(r)$  can be calculated from refractivity by the relation

$$n(r) = L \frac{\nu(r)}{\nu_{STP}} \quad (\text{A6})$$

where  $L$  is Loschmidt's number and  $\nu_{STP}$  is a reference value assumed constant by the assumption of a homogenous atmosphere. The equation of hydrostatic equilibrium and ideal gas law close the system to solve for pressure  $p(r)$ , temperature  $T(r)$  and scale height  $H(r)$ . The temperature-radius and pressure-radius results can be used to produce a temperature-pressure profile  $T(p)$ , which is removes the sensitivity to the geometrical solution from model fitting.

The integrals in Equations A1, A3, and A5 are mathematically accurate but idealized because we cannot integrate to infinity, which is why boundary conditions from model fitting are so important. The numerical form of these integrals shown in [Elliot, Person, & Qu \(2003\)](#) combines the results of model fitting and uses discrete sums.

Uncertainties reported from the model fitting routine are used as the starting point of covariance matrices calculated for each inversion step. The final reported uncertainties are highly sensitive to the model fit parameters because of the high correlation between successive inversion points. In the original procedure from [Elliot, Person, & Qu \(2003\)](#), the model fit is only carried out to the top portion of the light curve, before inversion begins. We modified that procedure to fit the entire light curve and then begin inversion as high up as possible to further minimize uncertainties.

Many of the inversion steps remain the same in the [Elliot, Person, & Qu \(2003\)](#) approach as that of [French et al. \(1978\)](#), with a couple key improvements. (1) Inversion is adapted for high performance computing and can process high resolution light curves. (2) Error propagation is done in a mathematically sound manner instead of the estimates used in the original work. For details of the error analysis, the reader is referred to Section 4 of [Elliot, Person, & Qu \(2003\)](#).

## REFERENCES

- 826 Abel, N. H. 1826, Journal für die reine und 857 Elliot, J. L., French, R. G., Dunham, E., et al.  
 827 angewandte Mathematik, 1, 153 858 1977a, Science, 195, 485  
 828 Ando, H., Imamura, T., & Tsuda, T. 2012, J. 859 —. 1977b, ApJ, 217, 661  
 829 Atmos. Sci., 69, 2906 860 Elliot, J. L., Person, M. J., & Qu, S. 2003, AJ,  
 830 Andrews, D. G., Leovy, C. B., & Holton, J. R. 861 126, 1041  
 831 1987, Middle atmosphere dynamics (Academic 862 Elliot, J. L., & Young, L. A. 1992, AJ, 103, 991  
 832 press) 863 England, S. L., Liu, G., Yiğit, E., et al. 2017, J.  
 833 Banfield, D., Spiga, A., Newman, C., et al. 2020, 864 Geophys. Res., 122, 2310  
 834 Nature Geoscience, 13, 190 865 Fazel-Rastgar, F. 2019, Ap&SS, 364, 54  
 835 Barnes, J. R., Haberle, R. M., Wilson, R. J., et al. 866 Feofilov, A. G., Kutepon, A. A., Rezac, L., &  
 836 2017, in The atmosphere and climate of Mars, 867 Smith, M. D. 2012, Icarus, 221, 949  
 837 ed. R. M. Haberle, R. T. Clancy, F. Forget, 868 Forget, F., Montmessin, F., Bertaux, J., et al.  
 838 M. D. Smith, & R. W. Zurek, 202–228 869 2009, J. Geophys. Res., 114, E01004,  
 839 Baum, W. A., & Code, A. D. 1953, AJ, 58, 108 870 10.1029/2008JE003086  
 840 Bosh, A. S., Person, M. J., Levine, S. E., et al. 871 French, R. G., & Elliot, J. L. 1979, Astrophys. J.,  
 841 2015, Icarus, 246, 237 872 229, 828  
 842 Chamberlain, D., & Elliot, J. 1997, PASP, 109, 873 French, R. G., Elliot, J. L., & Gierasch, P. J.  
 843 1170 874 1978, Icarus, 33, 186  
 844 Clancy, R. T., Sandor, B. J., Wolff, M. J., et al. 875 French, R. G., & Gierasch, P. J. 1974, Journal of  
 845 2000, J. Geophys. Res., 105, 9553 876 Atmospheric Sciences, 31, 1707  
 846 Creasey, J. E., Forbes, J. M., & Hinson, D. P. 877 French, R. G., & Taylor, G. E. 1981, Icarus, 45,  
 847 2006a, Geophys. Res. Lett., 33, L01803 878 577  
 848 Creasey, J. E., Forbes, J. M., & Keating, G. M. 879 Fritts, D. C., & Alexander, M. J. 2003, Rev.  
 849 2006b, Geophys. Res. Lett., 33, L22814, 880 Geophys., 41, 1003  
 850 10.1029/2006GL027583 881 Fritts, D. C., Wang, L., & Tolson, R. H. 2006, J.  
 851 Eckermann, S. D., Ma, J., & Zhu, X. 2011, Icarus 882 Geophys. Res., 111, A12304,  
 852 211, 429 883 10.1029/2006JA011897  
 853 Elliot, J., & Olkin, C. 1996, Annual Review of 884 Gilli, G., Forget, F., Spiga, A., et al. 2020, J.  
 854 Earth and Planetary Sciences, 24, 89 885 Geophys. Res., 10.1029/2018JE005873  
 855 Elliot, J. L., Dunham, E., & Church, C. 1976, 886 Gröller, H., Montmessin, F., Yelle, R. V., et al.  
 856 S&T, 52, 23 887 2018, J. Geophys. Res., 123, 1449

- 888 Gubenko, V. N., Kirillovich, I. A., & Pavelyev, 920 Person, M. J., Elliot, J. L., Gulbis, A. A. S., et al.  
 889 A. G. 2015, *Cosmic Research*, 53, 133 921 2008, *AJ*, 136, 1510
- 890 Heavens, N. G., Kass, D. M., Kleinböhl, A., & 922 Person, M. J., Dunham, E. W., Bosh, A. S., et al.  
 891 Schofield, J. T. 2020, *Icarus*, 341, 113630 923 2013, *AJ*, 146, 83
- 892 Holstein-Rathlou, C., Maue, A., & Withers, P. 924 Person, M. J., Bosh, A. S., Zuluaga, C. A., et al.  
 893 2016, *Planet. Space Sci.*, 120, 15 925 2019, *Icarus*, 113572
- 894 Holton, J. R. 2013, An introduction to dynamic 926 Quémérais, E., Bertaux, J.-L., Koralev, O., et al.  
 895 meteorology, fifth edition.. edn. (Amsterdam: 927 2006, *J. Geophys. Res.*, 111, E09S04,  
 896 Elsevier : Academic Press) 928 10.1029/2005JE002604
- 897 Houghton, J. 2002, The physics of atmospheres 929 Savitzky, A., & Golay, M. J. E. 1964, *Analytical  
 898 (Cambridge University Press) 930 Chemistry*, 36, 1627
- 899 Hubbard, W. B. 1982, *Adv. Space Res.*, 2, 103 931 Seiff, A., & Kirk, D. B. 1976, *Science*, 194, 1300
- 900 Keenan, P. C., & McNeil, R. C. 1989, *ApJS*, 71, 932 Siddle, A. G., Mueller-Wodarg, I. C. F., Stone,  
 901 245 933 S. W., & Yelle, R. V. 2019, *Icarus*, 333, 12
- 902 Kieffer, H. H., Jakosky, B. M., Snyder, C. W., & 934 Smith, M. D., Bouger, S. W., Encrénaz, T.,  
 903 Matthews, M. S. 1992, *Mars* 935 Forget, F., & Kleinböhl, A. 2017, in *The  
 904 Lemoine, F. G., Smith, D. E., Rowlands, D. D., 936 atmosphere and climate of Mars*, ed. R. M.  
 905 et al. 2001, *J. Geophys. Res.*, 106, 23359 937 Haberle, R. T. Clancy, F. Forget, M. D. Smith,  
 906 Magalhães, J. A., Schofield, J. T., & Seiff, A. 938 & R. W. Zurek, 20–41
- 907 1999, *J. Geophys. Res.*, 104, 8943 939 Smith, M. D., Pearl, J. C., Conrath, B. J., &  
 908 Millour, E., Forget, F., Spiga, A., et al. 2019, in 940 Christensen, P. R. 2001, *J. Geophys. Res.*, 106,  
 909 *Geophysical Research Abstracts*, Vol. 21 941 23929
- 910 Montabone, L., Forget, F., Millour, E., et al. 2015 942 Spiga, A., González-Galindo, F., López-Valverde,  
 911 Icarus, 251, 65 943 M. Á., & Forget, F. 2012a, *Geophys. Res. Lett.*,  
 912 Montmessin, F., Bertaux, J.-L., Quémérais, E., 944 39, L02201  
 913 et al. 2006, *Icarus*, 183, 403 945 —. 2012b, *Geophys. Res. Lett.*, 39, L02201  
 914 Mueller-Wodarg, I. C. F., Strobel, D. F., Moses, 946 Tellmann, S., Pätzold, M., Häusler, B., Hinson,  
 915 J. I., et al. 2008, *SSRv*, 139, 191 947 D. P., & Tyler, G. L. 2013a, *J. Geophys. Res.*,  
 916 Parish, H. F., Schubert, G., Hickey, M. P., & 948 118, 306  
 917 Walterscheid, R. L. 2009, *Icarus*, 203, 28 949 Tellmann, S., Pätzold, M., Häusler, B., Hinson,  
 918 Pasachoff, J. M., Person, M. J., Bosh, A. S., et al. 950 D. P., & Tyler, G. L. 2013b, *Journal of  
 919 2016, *AJ*, 151, 97 951 Geophysical Research (Planets)*, 118, 306

- 952 Terada, N., Leblanc, F., Nakagawa, H., et al. 967 Withers, P., & Smith, M. D. 2006, Icarus, 185, 133  
953 2017, J. Geophys. Res., 122, 2374  
954 Vals, M., Spiga, A., Forget, F., et al. 2019, Planet. 968 Withers, P., Towner, M. C., Hathi, B., & Zarnecki,  
955 Space Sci., 178, 104708 969 J. C. 2003b, Planet. Space Sci., 51, 541  
956 Wasserman, L. H., & Veverka, J. 1973, Icarus, 20, 970 Wright, C. J. 2012, Icarus, 219, 274  
957 322  
958 Withers, P. 2006, Geophys. Res. Lett., 33, L02201 971 Yiğit, E., & Medvedev, A. S. 2015, Adv. Space  
959 —. 2013, American Journal of Physics, 81, 565 972 Res., 55, 983  
960 Withers, P., Bougner, S. W., & Keating, G. M. 973 Yiğit, E., England, S. L., Liu, G., et al. 2015,  
961 2003a, Icarus, 164, 14 974 Geophys. Res. Lett., 42, 8993  
962 Withers, P., & Catling, D. C. 2010, Geophys. Res. 975 Young, A. T. 1967, AJ, 72, 747  
963 Lett., 37, L24204, 10.1029/2010GL045382  
964 Withers, P., Pratt, R., Bertaux, J.-L., &  
965 Montmessin, F. 2011, J. Geophys. Res., 116,  
966 E11005, 10.1029/2011JE003847

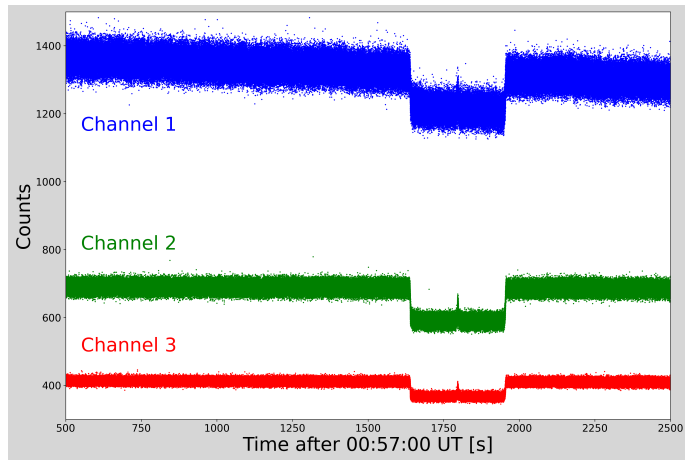


**Figure 1.** Raw data obtained from data storage device. Original resolution of 4 ms is plotted versus arbitrary electron counts. The upper baseline in Channel 1 has a clear negative trend that was fit to a line and corrected. Similar corrections were performed on the other channels.

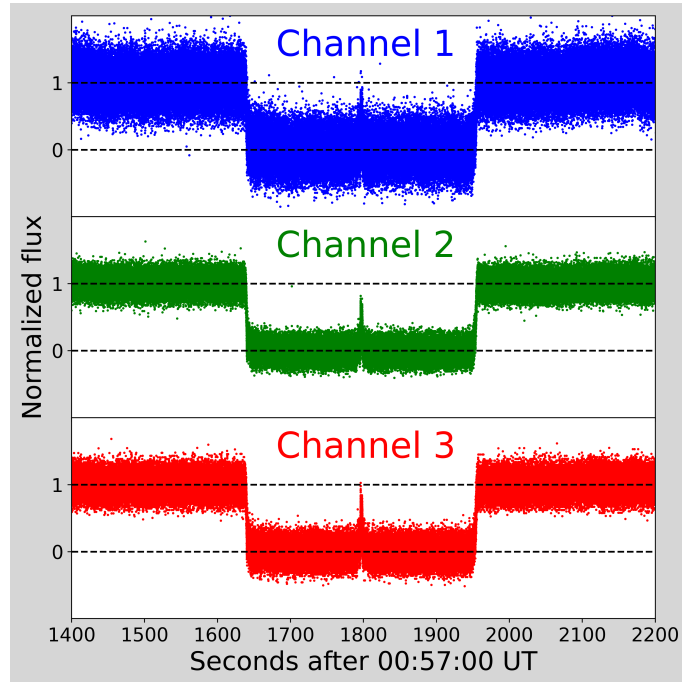


**Figure 2.** Normalized light curves of all three channels. Flux level is set to 1.0 at upper baseline and 0.0 at lower baseline, approximating no residual refraction around the limb away from immersion, emersion, and the central flash. The central flash in all three channels has two unequal peaks, not visible at this scale.

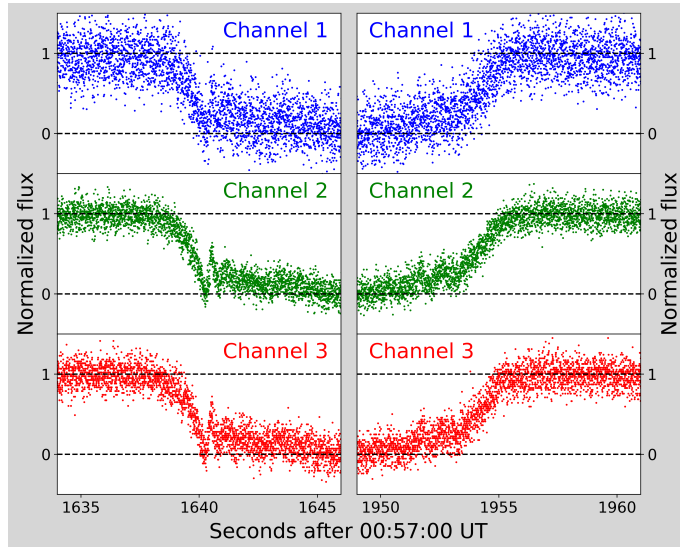


**Figure 3.** As in Figure 2, zoomed in on immersion and emersion. Here it is possible to see that channel 1 has much lower signal-to-noise than channels 2 and 3. Features of note include the prominent spikes and asymmetry of the profiles.

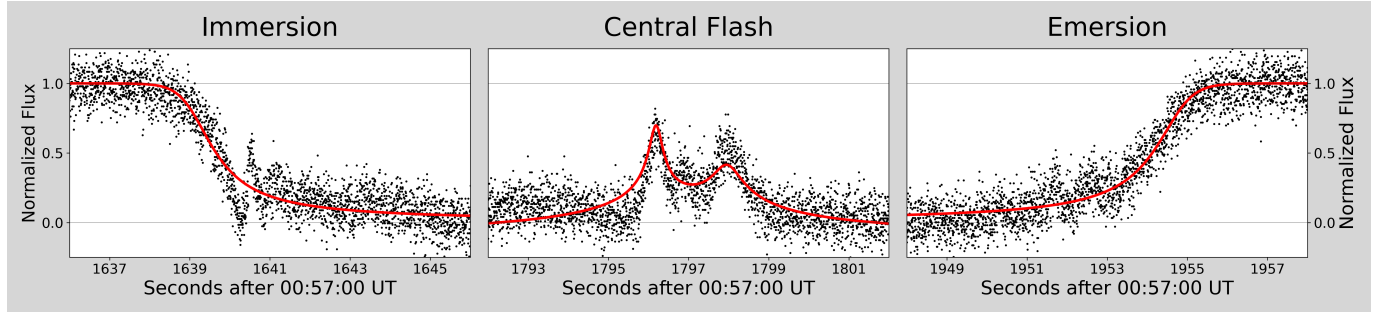


**Figure 4.** Isothermal model fits to immersion, central flash, and emersion curves following the Elliot & Young (1992) models. These model fits were used to set the upper boundary conditions at the start of inversion at 0.9 flux. The central flash fit was used to solve the event geometry for the impact parameter.

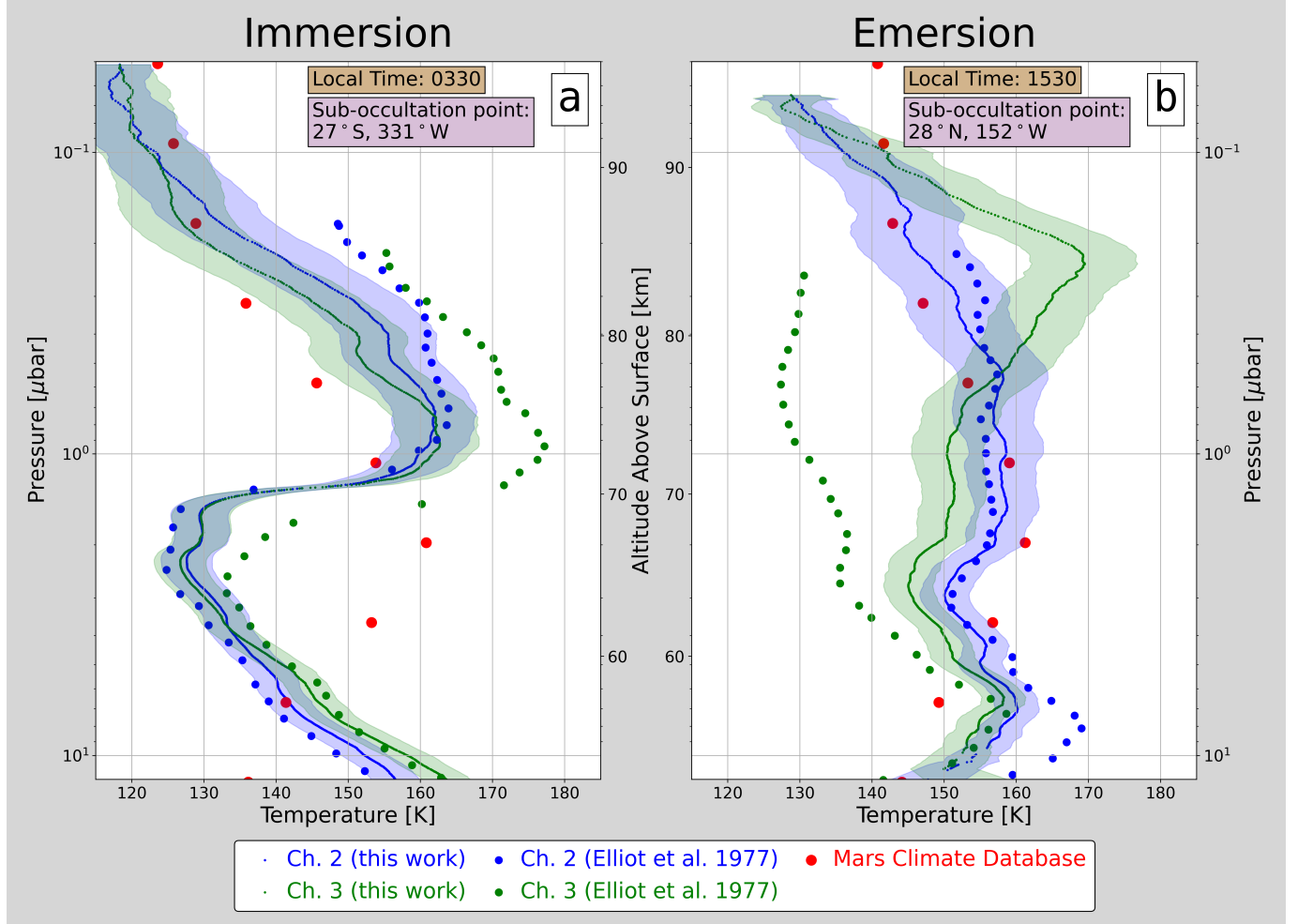


**Figure 5.** Temperature profiles of the middle Martian atmosphere. Reanalysis results in full resolution are compared to the original profiles of Elliot et al. (1977b) as well as the Mars Climate Database. The local Martian time of each profile and the surface sub-occultation point are indicated. The shaded regions represent uncertainty in temperature shifts of the entire profile because adjacent inversion results are highly correlated. The pressure scale is exact for all data being compared, but the altitude scale is approximate (See Section 6.1).

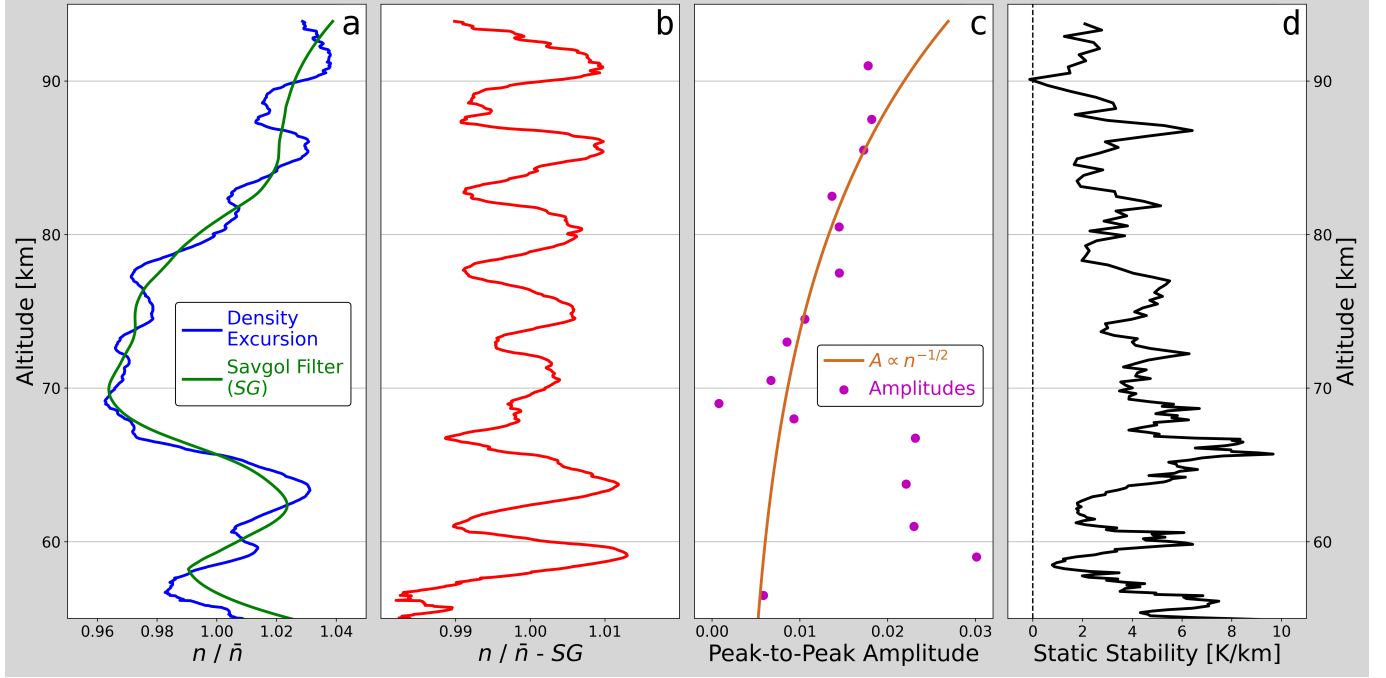


**Figure 6.** Occultation emersion channel 2. a. Density excursion (blue) resulting from dividing the density profile ( $n$ ) by the exponential atmospheric model ( $\bar{n}$ ). Small-scale waves and large waves (thermal tides) are superimposed, which motivated using the savgol filter ( $SG$ ; green) to isolate just the small-scale waves. b. The extracted small-scale wave, resulting from subtracting the savgol filter with 10 km filter window from the density excursion. c. Peak-to-peak amplitudes of the extracted wave (magenta). A model of gravity wave amplitude growth (Mueller-Wodarg et al. 2008) is overlaid (orange) to fit the amplitudes above 68 km altitude. d. Static stability determined by Equation 3. Altitudes where static stability decrease below or near zero, such as around 58 km and 90 km, indicate regions of the atmosphere that may have wave breaking.

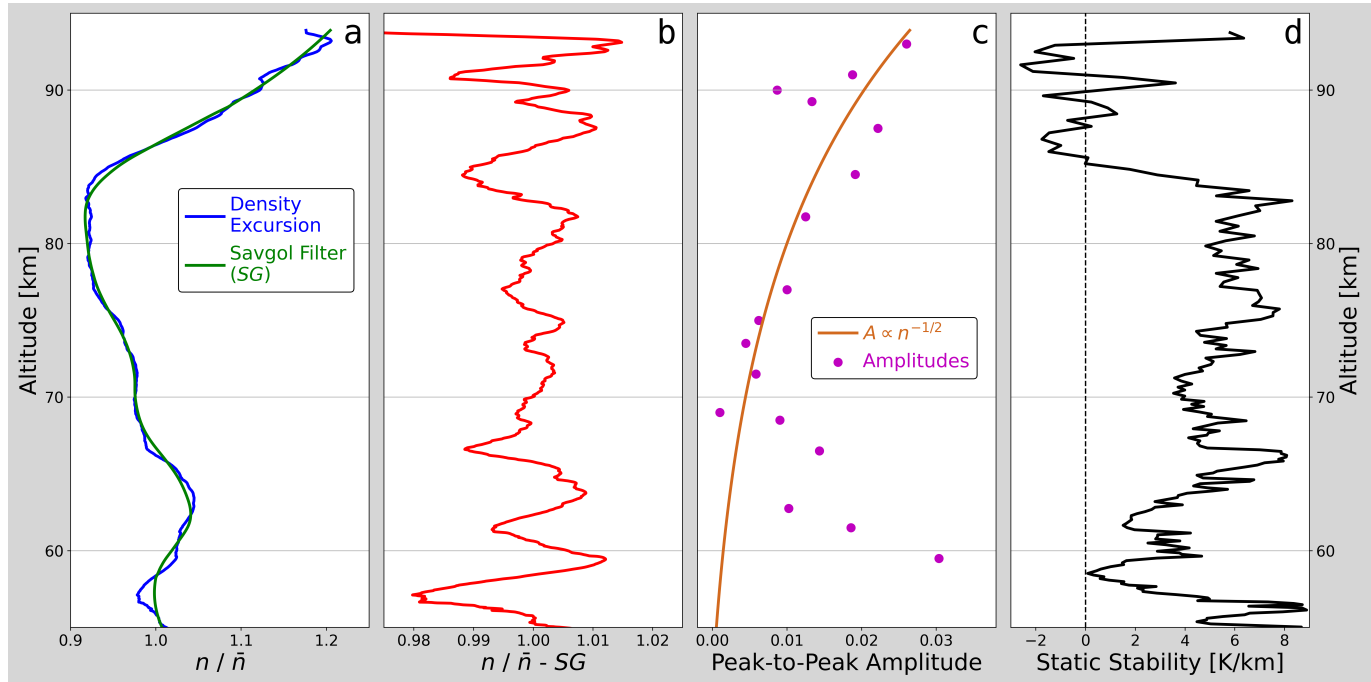


**Figure 7.** Occultation emersion channel 3 as in Figure 6.

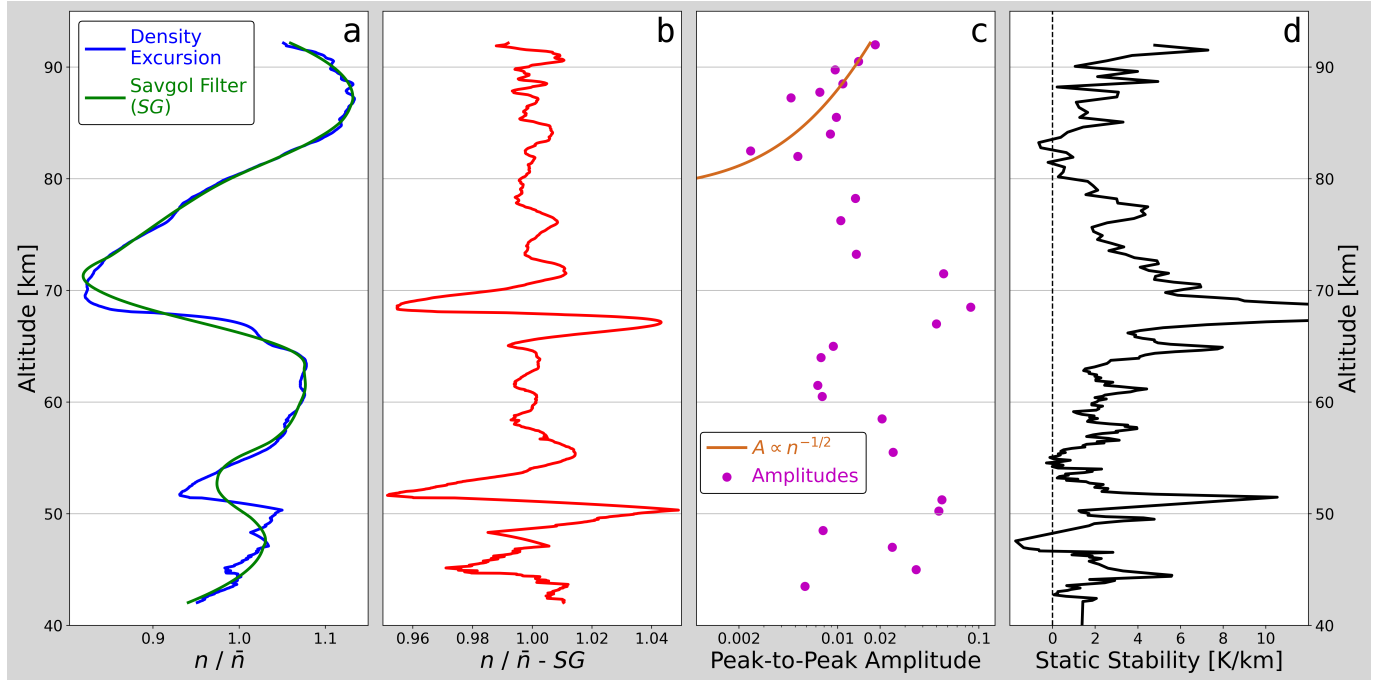


**Figure 8.** Occultation immersion channel 2 as in Figure 6.

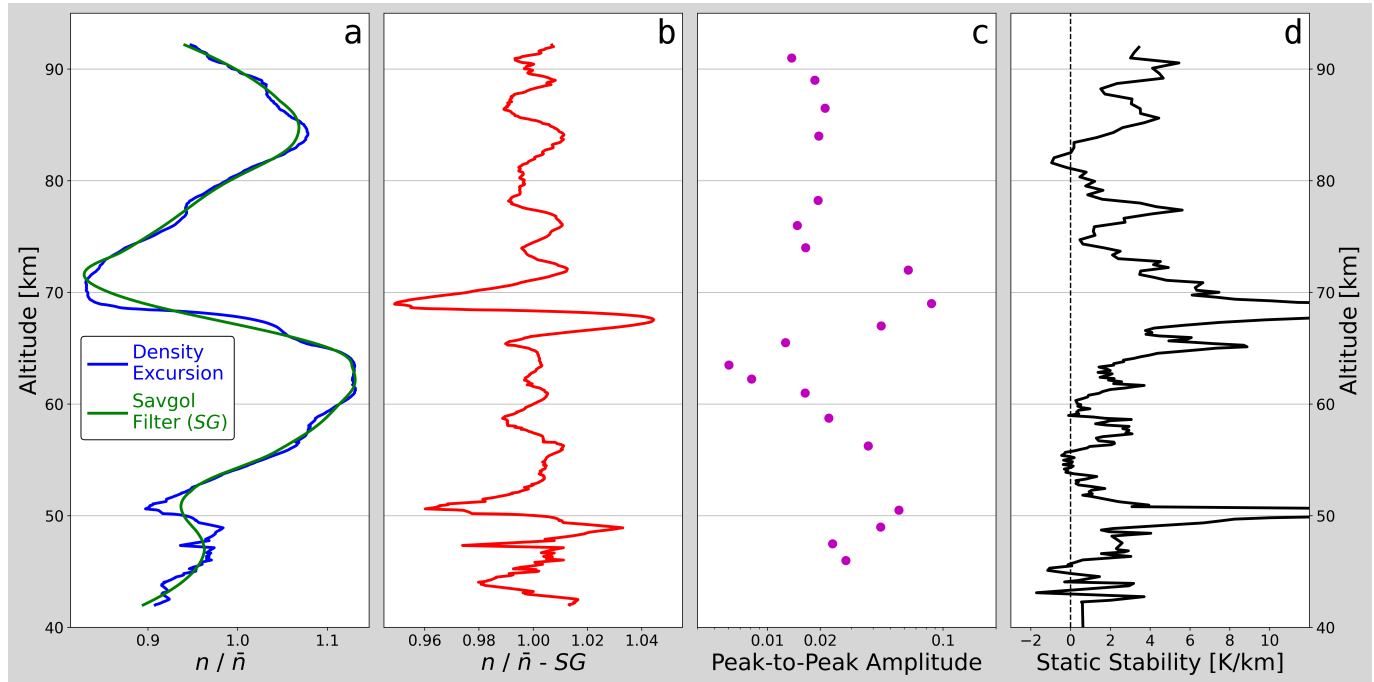


**Figure 9.** Occultation immersion channel 3 as in Figure 6.

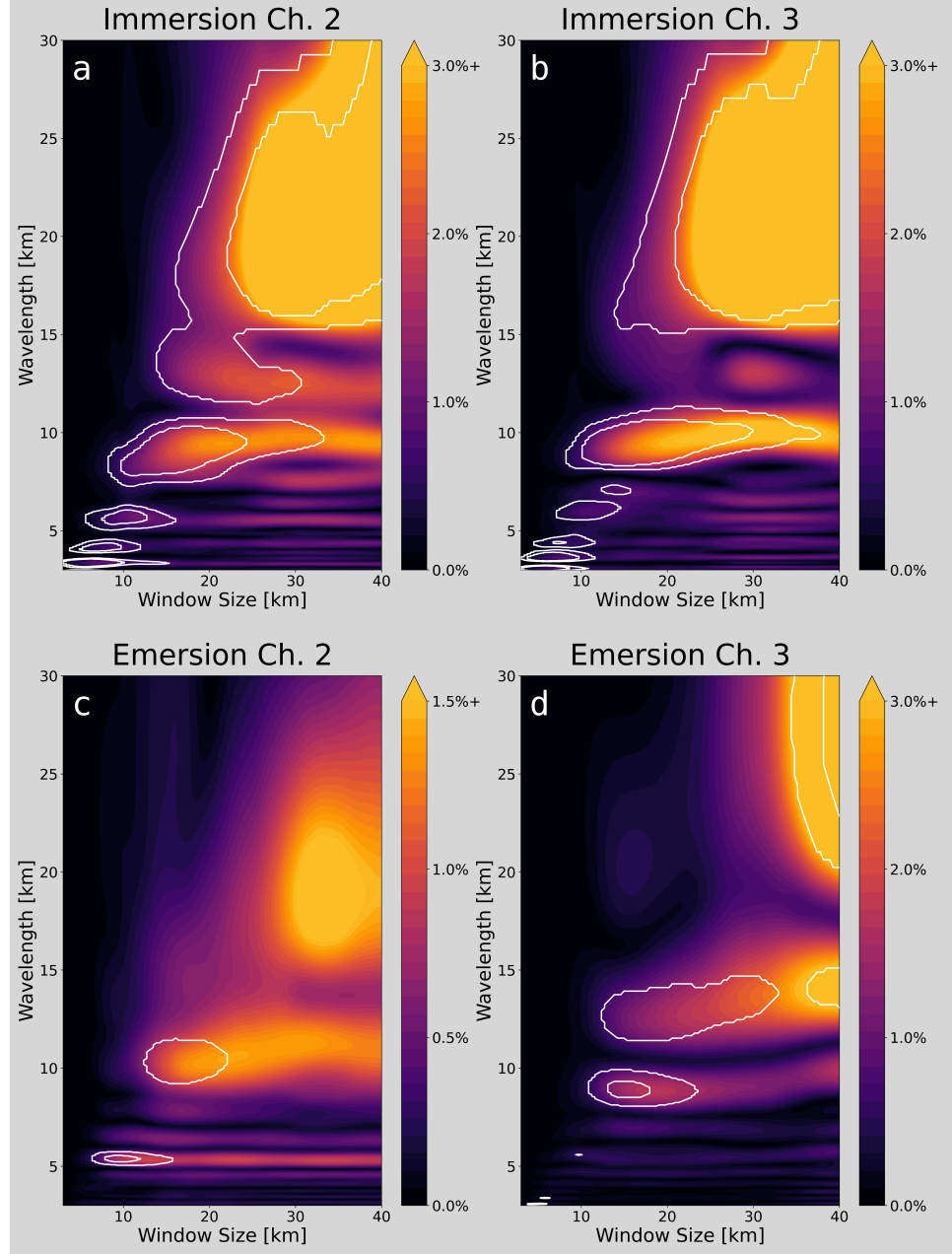


**Figure 10.** Amplitude spectra of all four occultation profiles represented as a contour plot. The x-axis is savgol filter window size, and y-axis is vertical wavelength of modes in the sample. The colored contour levels are wave amplitudes. The white contour lines indicate confidence intervals of the detected amplitudes, determined from a control test (see Section 8.1). The outer line is a 95% confidence and the inner line is 99.99% confidence.

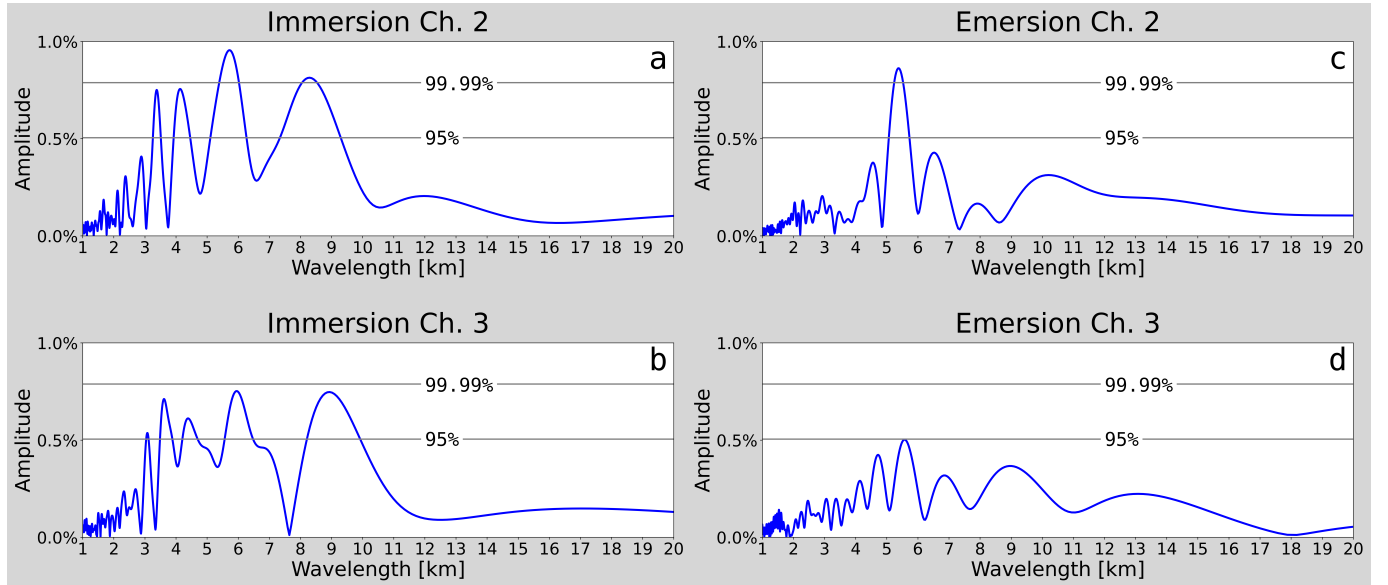


**Figure 11.** Amplitude spectra for occultation profiles with a savgol filter window of 10 km. Confidence intervals of 95% and 99.99% are indicated. Each spectrum is a slice through the corresponding two-dimensional panel in Figure 10 at a window size of 10 km.

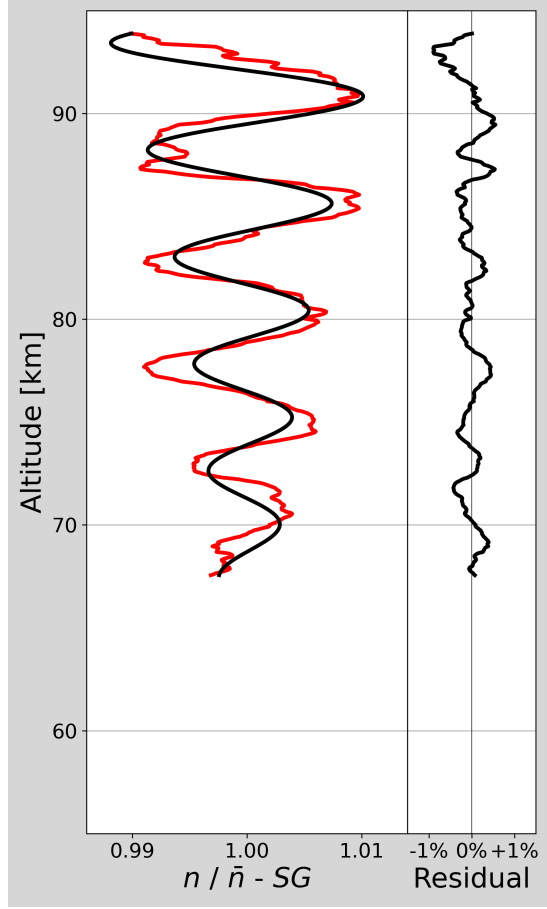


**Figure 12.** Extracted wave in Figure 6b (red) overlaid with the gravity model in Equation 4 (black). The fit is illustrative only. Residuals are computed *data minus model* and are given in percent. The reasonable quality of this fit offers further evidence that propagating gravity waves are responsible for the density perturbations we observe.

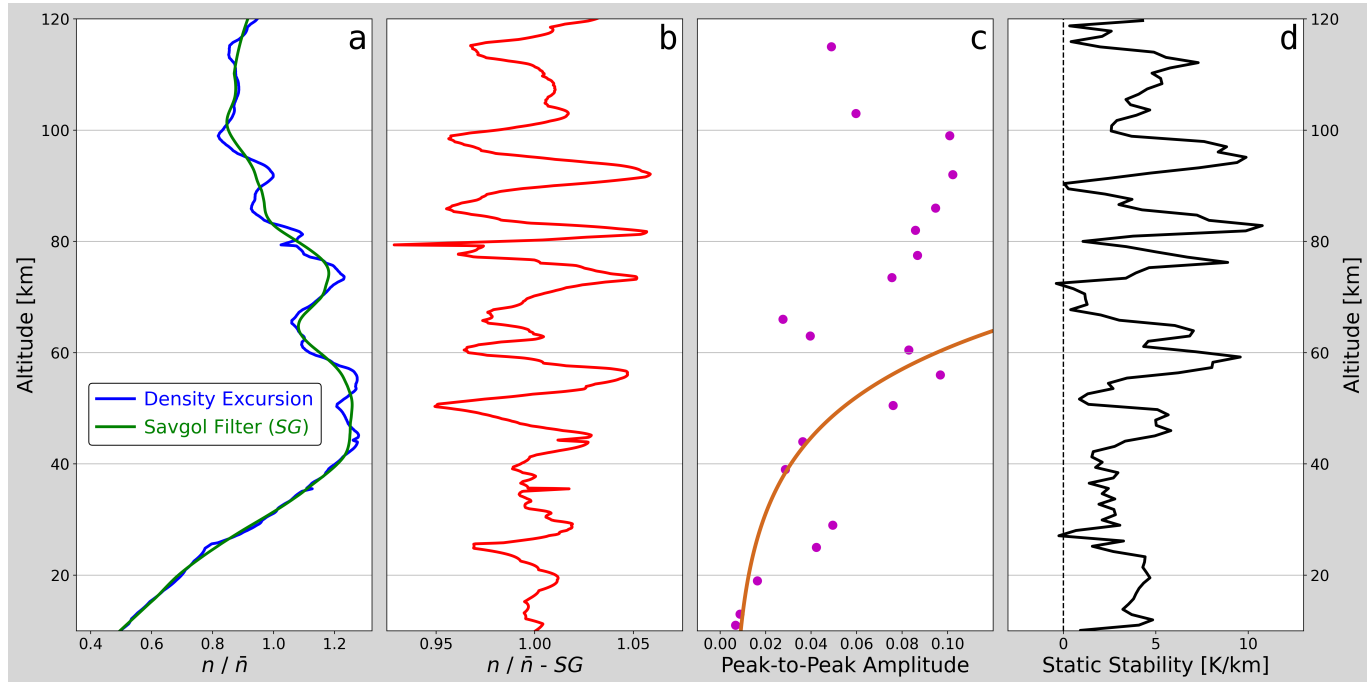


**Figure 13.** Viking 1 primary wave results as in Figure 6 with a 20 km savgol filter window.

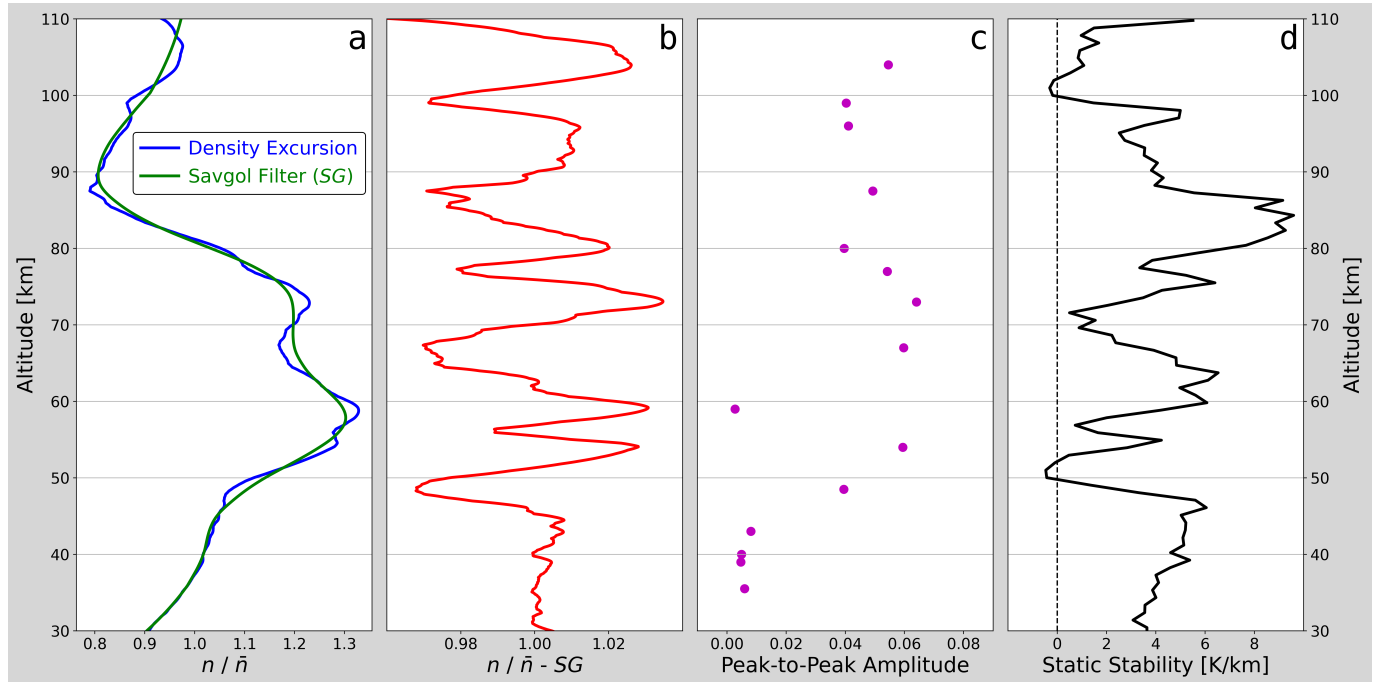


**Figure 14.** Viking 2 primary wave results as in Figure 6 with a 20 km savgol filter window.

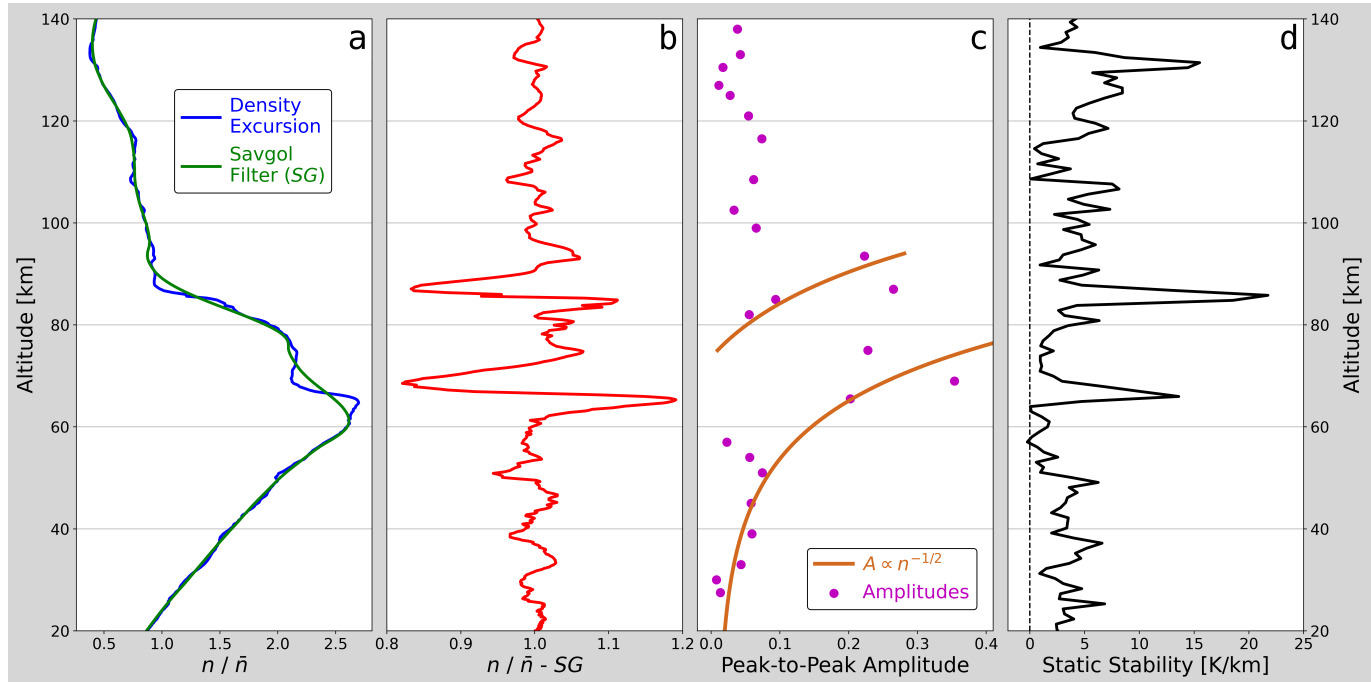


**Figure 15.** Pathfinder primary wave results as in Figure 6 with a 20 km savgol filter window.

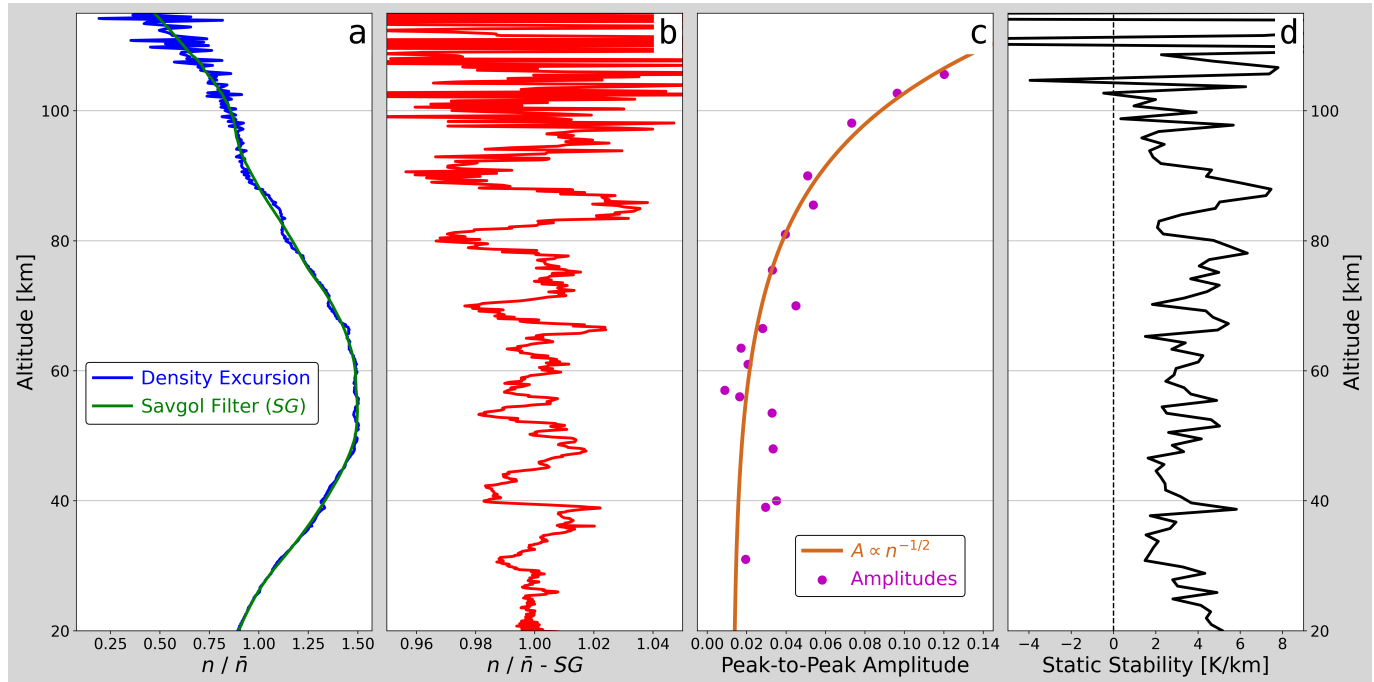


**Figure 16.** Spirit primary wave results as in Figure 6 with a 20 km savgol filter window.

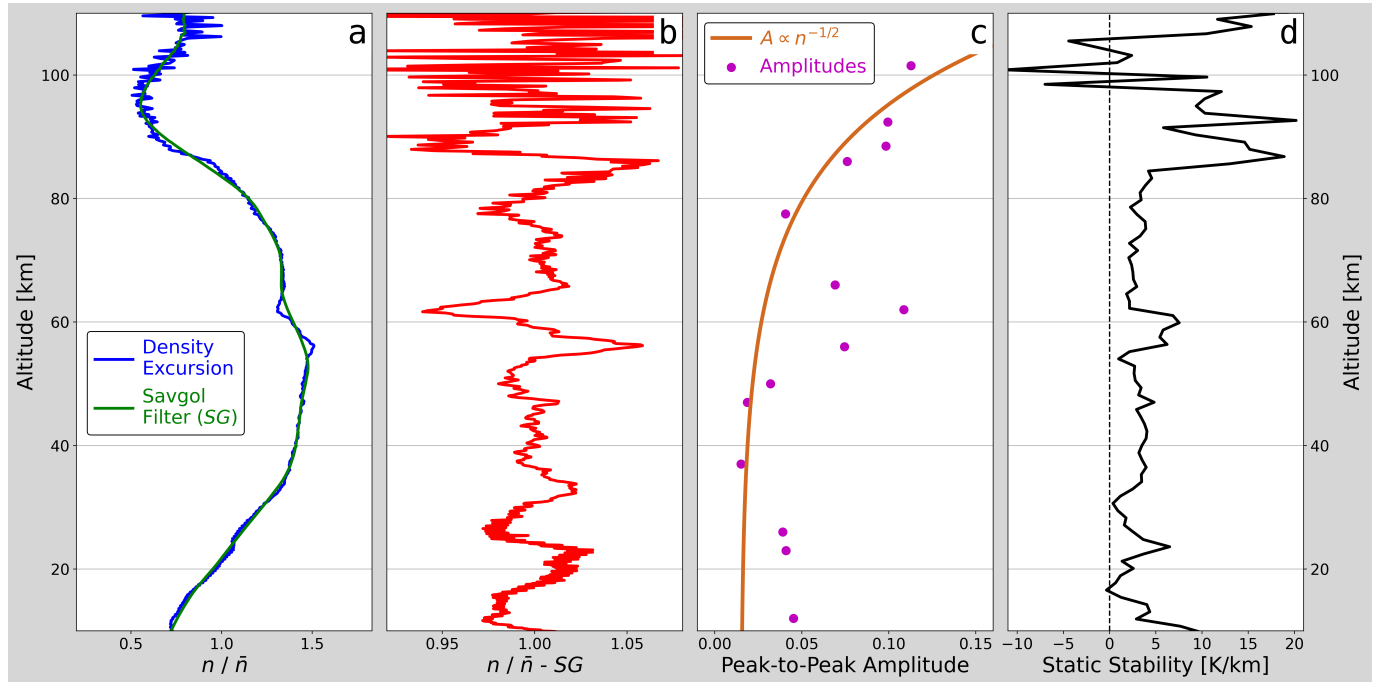


**Figure 17.** Opportunity primary wave results as in Figure 6 with a 20 km savgol filter window.

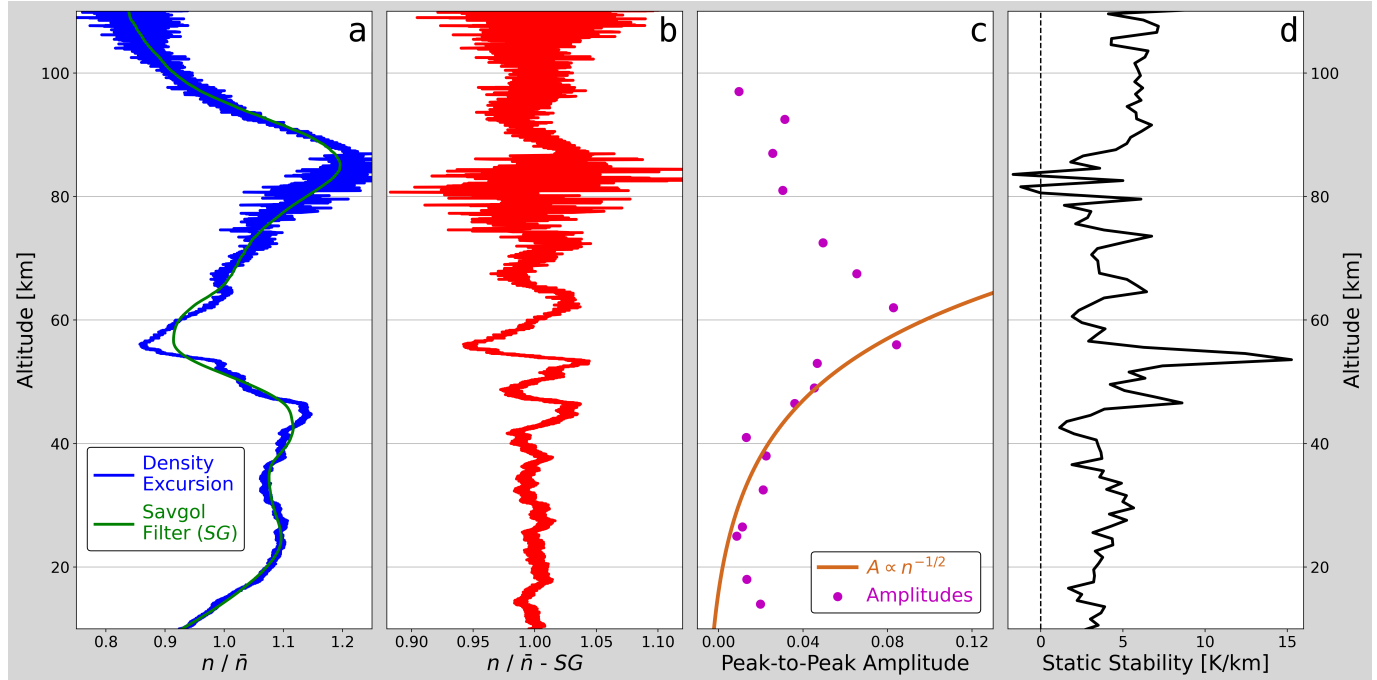


**Figure 18.** Phoenix primary wave results as in Figure 6 with a 20 km savgol filter window.

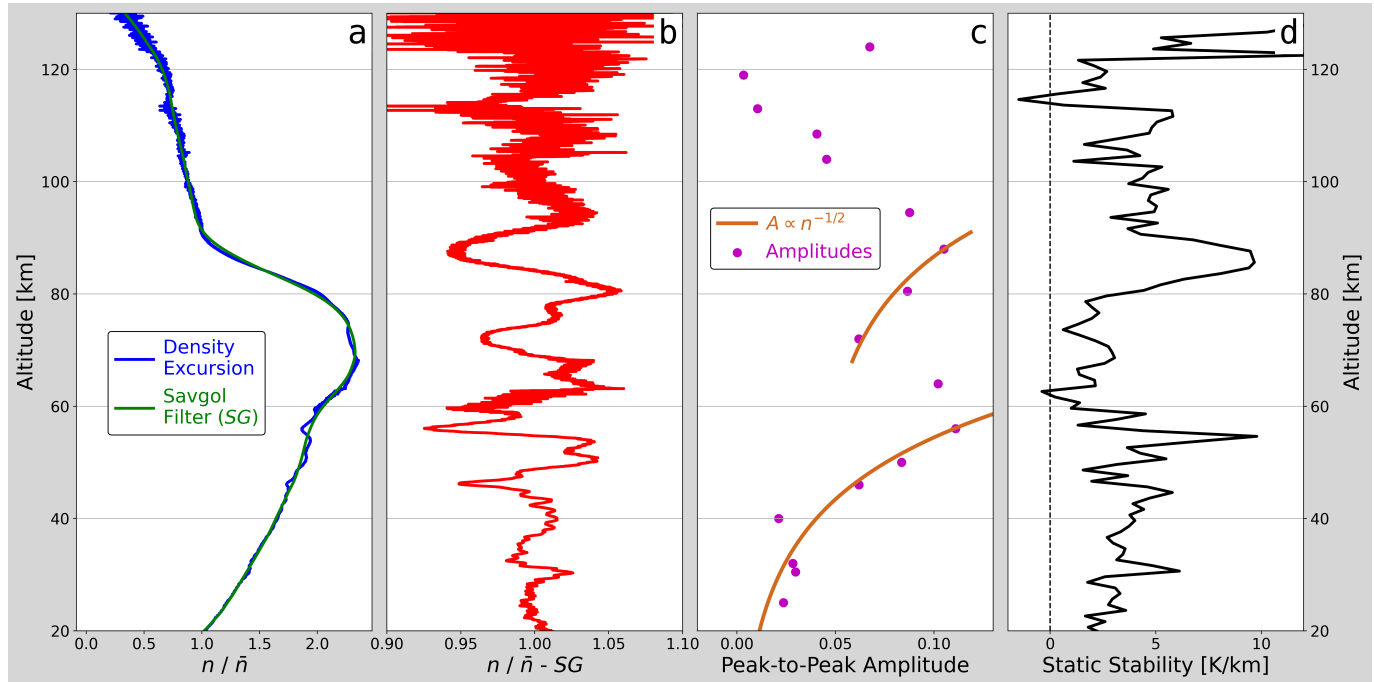


**Figure 19.** Curiosity primary wave results as in Figure 6 with a 20 km savgol filter window.

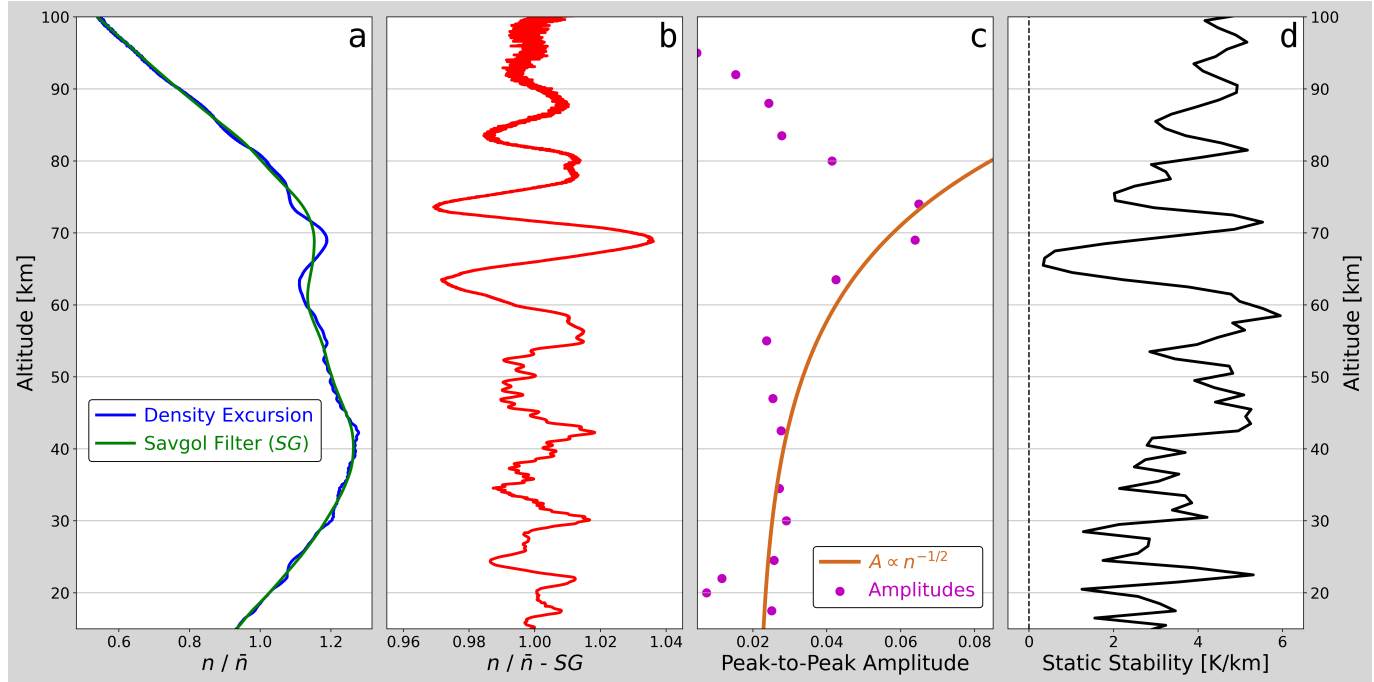


**Figure 20.** InSight primary wave results as in Figure 6 with a 20 km savgol filter window.

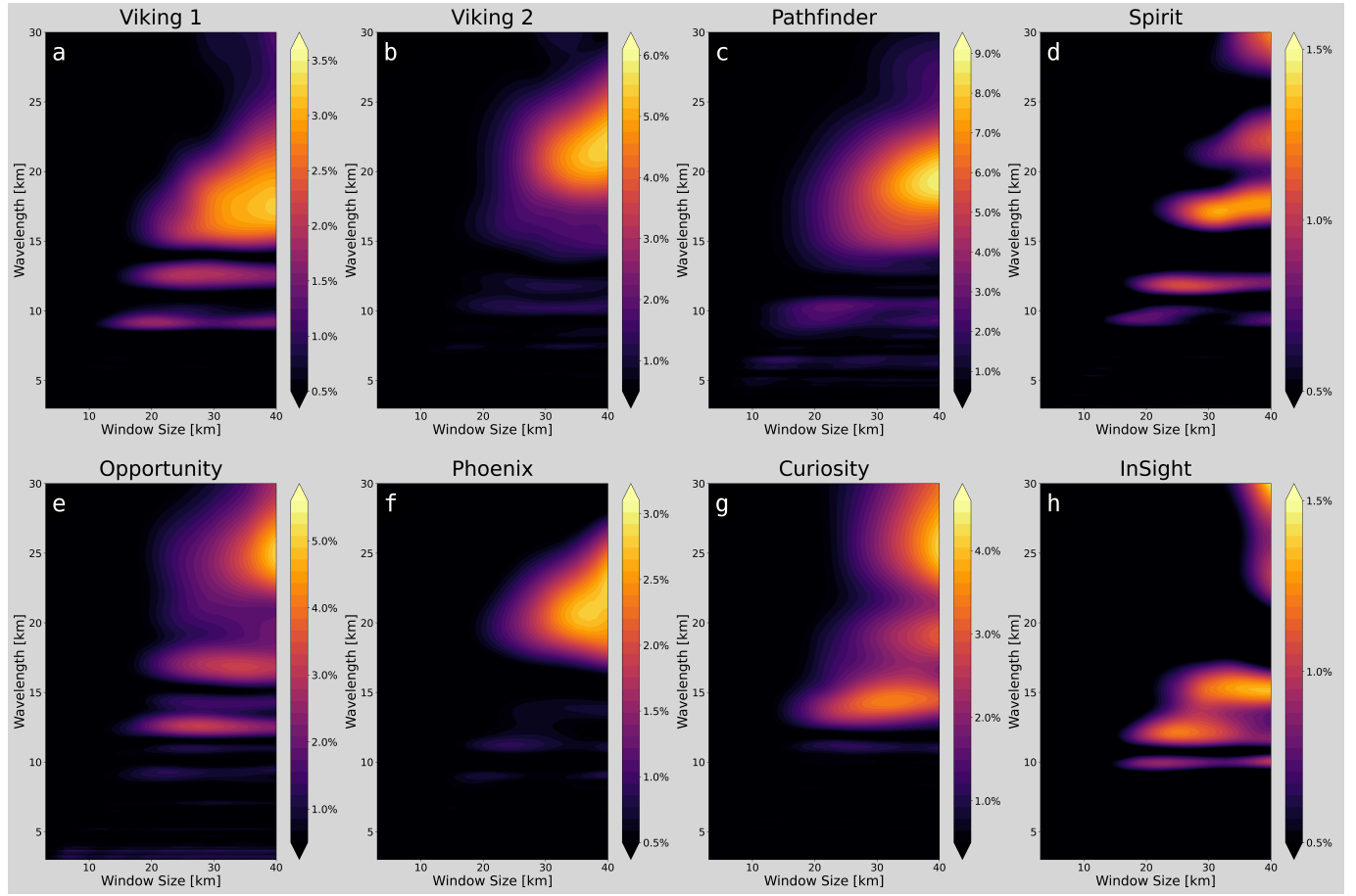


**Figure 21.** Amplitude spectra of all eight entry profiles represented as a contour plot, as in Figure 10. The features of wavelength greater than 15 km are likely thermal tides. The features of greatest interest are resolved best with a window size of 20 km.

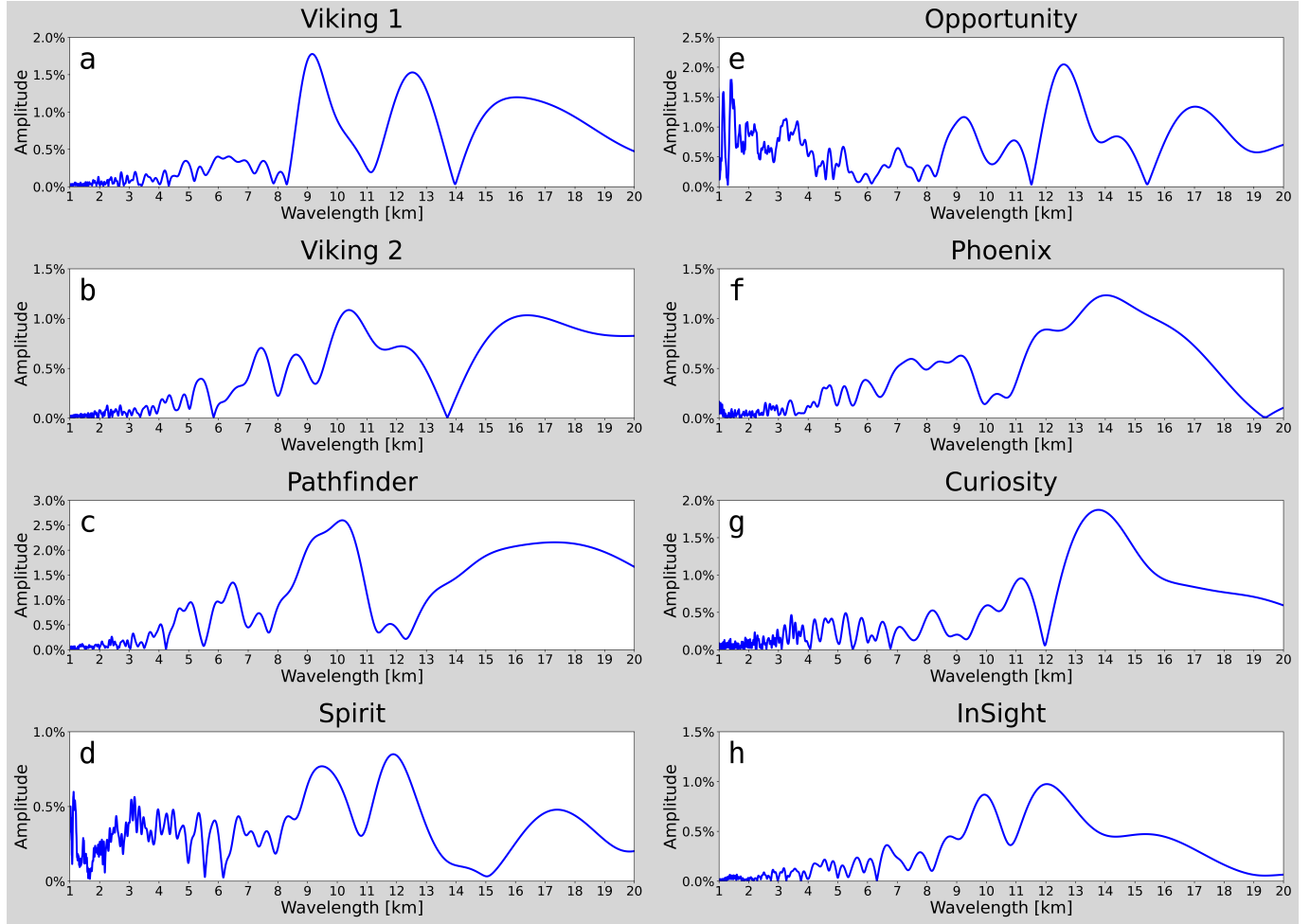


**Figure 22.** Amplitude spectra for all entry profiles with a savgol filter window of 20 km. The 20 km window highlights features representative of small-scale atmospheric waves. Dominant patterns in the amplitude spectra include peak wavelengths in the range 9–14 km, single- and double-peaked features, and peak amplitudes in the range 1–3%.

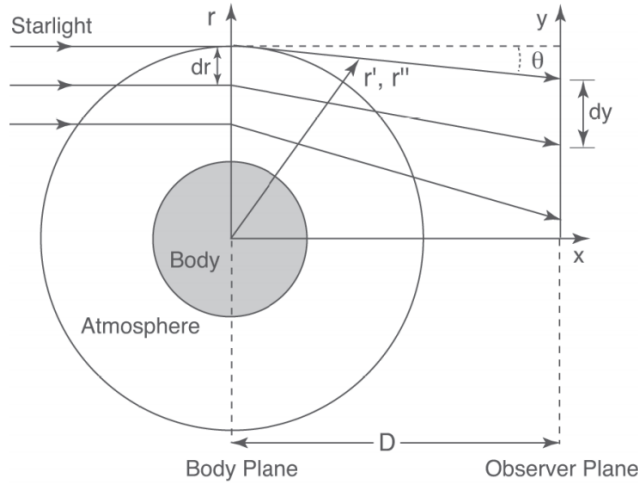


**Figure 23.** Refraction of starlight through a small body atmosphere. In this frame of reference, the target body is stationary and the star and observer move. The rays of starlight passing through spherical shells of the occulting body's atmosphere at radius  $r$  bend by angle  $\theta$  before being observed on the right side of the diagram at relative observer distance  $y$ . The observer-body separation is given by  $D$ .  $r'$  and  $r''$  serve as variables of integration. From [Elliot, Person, & Qu \(2003\)](#).

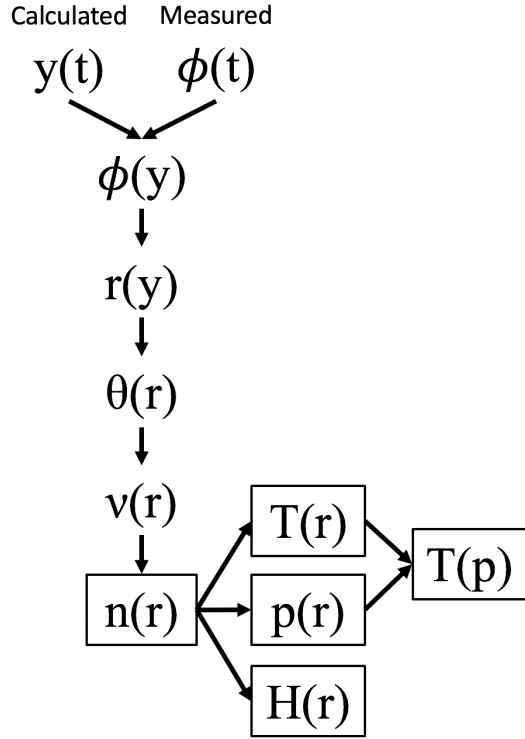


**Figure 24.** Flowchart showing the steps of inversion. Observer position  $y(t)$  is determined as a function of time from the occultation geometry and flux  $\phi(t)$  is measured as a time series. The important atmospheric properties are boxed: number density  $n(r)$ , temperature  $T(r)$ , pressure  $p(r)$  and scale height  $H(r)$  as a function of radius, and temperature as a function of pressure  $T(p)$ . After [Elliot, Person, & Qu \(2003\)](#).

**Table 1.** Conditions During Obtained Data Acquisition

Data Source	Date and Time	Latitude <sup>a</sup>	Longitude <sup>b</sup>	L <sub>s</sub> <sup>c</sup>	Local Time
		degrees	degrees	degrees	
Viking 1 <sup>d</sup>	1976-07-20 11:53:06	22.70	-48.22	97.2	14:25:46
Viking 2 <sup>d</sup>	1976-09-03 22:37:50	48.27	-225.99	117.9	13:03:54
Pathfinder <sup>e</sup>	1997-07-04 16:36:50.172	19.33	-33.55	143.0	08:22:56
Spirit <sup>f</sup>	2004-01-04 04:19:53.974	-14.57	175.48	327.9	12:25:12
Opportunity <sup>f</sup>	2004-01-25 04:48:43.605	-1.95	354.47	339.4	11:07:55
Phoenix <sup>g</sup>	2008-05-25 23:30:47.918	68.15	-125.90	76.9	11:34:50
Curiosity <sup>h</sup>	2012-08-06 05:10:42.924	-4.59	137.44	151.0	14:03:07
InSight <sup>i</sup>	2018-11-26 19:39:03.3441	4.50	135.62	296.0	03:42:26
Occultation Immersion <sup>j</sup>	1977-04-08 00:57:19.68	-27	-331	51.6	03:30
Occultation Emersion <sup>j</sup>	1977-04-08 01:02:34.01	28	-152	51.6	15:30

<sup>a</sup> Positive is East.

<sup>b</sup> Positive is North.

<sup>c</sup> Planetocentric Longitude of the Sun.

<sup>d</sup> Seiff & Kirk (1976)

<sup>e</sup> Magalhães et al. (1999)

<sup>f</sup> Withers & Smith (2006)

<sup>g</sup> Withers & Catling (2010)

<sup>h</sup> Holstein-Rathlou et al. (2016)

<sup>i</sup> Banfield et al. (2020)

<sup>j</sup> Elliot et al. (1977b)

**Table 2.** Model Fitting Parameter Results

Curve	Scale Height km	Temperature K	Ellipticity	Impact Parameter km	Reduced $\chi^2$
Immersion	$8.29 \pm 0.29$	$154.8 \pm 5.41$	-	-	0.962
Emersion	$6.55 \pm 0.26$	$122.3 \pm 4.86$	-	-	1.034
Central flash	-	-	$2.53 \times 10^{-3} \pm 6.8 \times 10^{-5}$	$22.1 \pm 0.23$	1.271

**Table 3.** Detected Wave Peaks

Profile	Wavelength	Peak Amplitude
km		
Immersion Ch. 2	3.4 <sup>a</sup>	0.93%
	4.1 <sup>a</sup>	0.70%
	5.7 <sup>a</sup>	1.1%
	9.4 <sup>a</sup>	2.7%
	12.5 <sup>b</sup>	2.2%
Immersion Ch. 3	3.4 <sup>a</sup>	0.61%
	4.1 <sup>a</sup>	0.94%
	6.1 <sup>b</sup>	0.82%
	10.0 <sup>a</sup>	3.4%
Emersion Ch. 2	5.4 <sup>a</sup>	0.93%
	10.3 <sup>b</sup>	1.4%
Emersion Ch. 3	5.6 <sup>b</sup>	0.50%
	8.9 <sup>a</sup>	1.6%
	13.7 <sup>a</sup>	2.4%
Viking 1	9.2	1.8%
	12.5	1.5%
	16.0	1.2%
Viking 2	10.4	1.1%
	16.4	1.0%
Pathfinder	10.2	2.6%
	17.3	2.2%
Spirit	9.5	0.77%
	11.9	0.85%
Opportunity	9.2	1.2%
	12.6	2.0%
	17.0	1.3%
Phoenix	9.0	0.75%
	11.2	0.79%
	19.6	0.72%
Curiosity	11.2	0.96%
	13.8	1.9%
InSight	9.9	0.87%
	12.0	0.98%

<sup>a</sup> Confidence of  $\geq 95\%$ .<sup>b</sup> Confidence of  $\geq 99.99\%$ .